CHALMERS
UNIVERSITY OF TECHNOLOGY

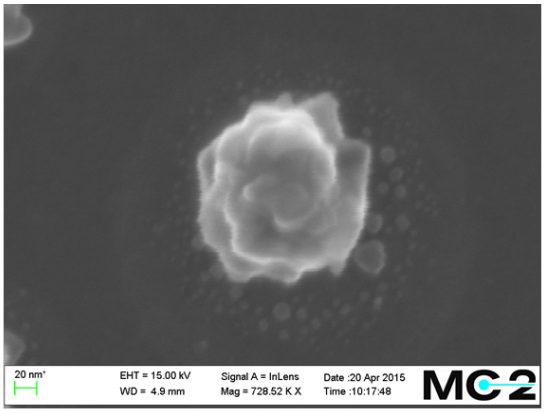

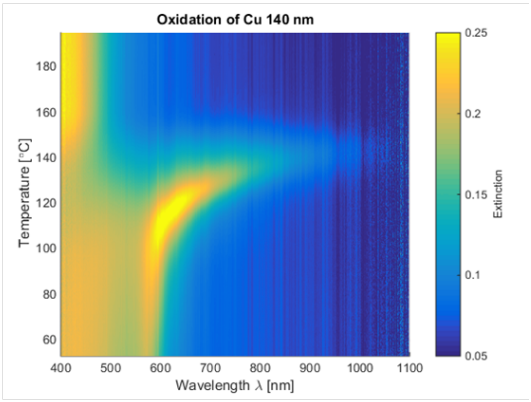

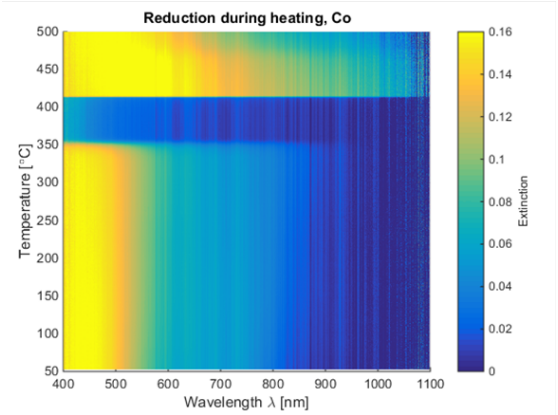

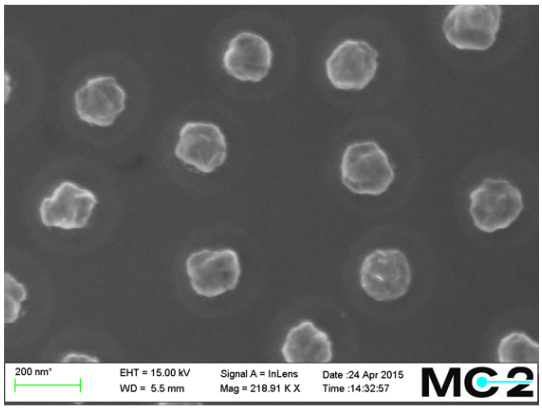

Nanoplasmonic Sensing of Transition Metal Catalyst Nanoparticle Oxidation States

Master's thesis in Applied Physics

DAVID JOHANSSON

Department of Applied Physics
CHALMERS UNIVERSITY OF TECHNOLOGY
Gothenburg, Sweden 2015

Master's thesis 2015

Nanoplasmonic Sensing of Transition Metal Catalyst Nanoparticle Oxidation States

DAVID JOHANSSON

CHALMERS
UNIVERSITY OF TECHNOLOGY

Department of Applied Physics
Division of Chemical Physics
Chalmers University of Technology
Gothenburg, Sweden 2015

Nanoplasmonic Sensing of Transition Metal Catalyst Nanoparticle Oxidation States
DAVID JOHANSSON

© DAVID JOHANSSON, 2015.

Supervisor: Ferry Nugroho, Division of Chemical Physics
Examiner: Christoph Langhammer, Division of Chemical Physics

Master's thesis 2015
Department of Applied Physics
Division of Chemical Physics
Chalmers University of Technology
SE-412 96 Gothenburg
Telephone +46 31 772 1000

Cover: Upper left: SEM image of a Cu nanoparticle exposed to nine cycles of oxygen and hydrogen, upper right: optical spectra of Cu nanoparticles exposed to oxygen during heating, lower left: optical spectra of Co nanoparticles exposed to hydrogen during heating, lower right: SEM image of Co nanoparticles exposed to hydrogen.

Typeset in LaTeX
Printed by [Name of printing company]
Gothenburg, Sweden 2015

Nanoplasmonic Sensing of Transition Metal Catalyst Nanoparticle Oxidation States
DAVID JOHANSSON
Department of Applied Physics
Chalmers University of Technology

Abstract

Catalysis is an important and key part of many processes both in fundamental research and in the applied chemical industry. The oxidation and reduction of transition metal catalysts are common reactions that affect the catalytic performance of the corresponding nanoparticles. Hence it is very important to understand the role of the oxidation state in a catalytic process, as well as to control it in order to maximize catalyst performance towards the formation of the desired product(s).
In this study copper and cobalt nanoparticle catalysts of sizes 67-190 nm were studied *in situ* with direct and indirect plasmonic sensing in temperature-programmed oxidation and reduction experiments. The experimental study proved, together with computational simulations with the Modified Long Wavelength Approximation, that the oxidation of copper yields a distinct change of the optical spectrum of the nanoparticles, and their exposure to 2 vol% O_2 in 200°C will mainly form Cu_2O. The oxidation and reduction process of copper was also found to be reversible, and the temperature for the two processes was found to slightly decrease over the reaction cycles, due to structural changes of the particles.

The outcome of the temperature-programmed oxidation and reduction experiments of cobalt nanoparticles was in several ways different from the copper ones. The most significant difference was that a broad dramatic change in extinction during the reduction process for the temperatures around 310-360°C was found. It was concluded that the effect was a combinatory result of a martensitic transformation, which simultaneously induced an increased oxidation rate of the cobalt oxides Co_2O_3 or CoO, as well as gives rise to a decrease of the conductivity.

Keywords: Localized plasmonic resonance, heterogeneous catalysis, nanoparticle sensing, copper, cobalt, oxidation, reduction

Acknowledgements

At first I want to thank my examiner **Christoph Langhammer** for giving me the opportunity to perform this thesis. For all the input, theoretical discussions, feedback and interest in this work. You inspire me!

I also want to thank **Ferry Nugroho**, my practical coach and supervisor, for teaching me the laboratory processes and for giving me inputs to the work, and **Carl Wadell** for always being there when I needed help with troubleshooting.

My friend and fellow worker, **David Albinsson**, for all support, discussions, lunch breaks, coffee time, fika and chit chat. This work would not have been so much fun without you!

Kristof Lodewijks for your initial inputs in the discussions about Co deposition in the cleanroom. **Björn Wickman**, **Lars Ilver**, and **Anna Clemens** for the guidance of the XPS machine, and how to translate the experimental results. **Igor Zoric** for insightful discussions of copper and cobalt properties. **Jenny Andersson** for giving support of the work both practically and theoretically, and for the welcoming demonstration of the laboratory. **Adriana Trinchero** for her competence in coffee, and for showing me how to prepare the best ones (espresso and hot skimmed milk), I would not have completed this thesis without that knowledge.

The rest of the **Chemical Physics group**, thanks for this time. I have had a wonderful and exciting time at this division.

Lovisa Nilebo, my love, for your support during these years. Thank you for being you.

David Johansson, Gothenburg, June 2015

Contents

1 Introduction **1**
1.1 Purpose of the project . . . 2

2 Plasmonic resonance **3**
2.1 Surface plasmons . . . 4
2.2 Localized surface plasmons . . . 4
2.3 Decay of LSPR . . . 6
2.4 Application of plasmonics . . . 6
2.5 Optical characterization . . . 7
2.5.1 Direct and indirect nanoplasmonic sensing . . . 8

3 Heterogeneous catalysis **11**
3.1 Catalysis . . . 11
3.2 Nanoparticles . . . 12
3.3 Materials used in this study and their key propertis . . . 13
3.3.1 Cu . . . 13
3.3.2 Co . . . 14

4 Methods **17**
4.1 Fabrication . . . 17
4.1.1 Hole-mask colloidal lithography . . . 17
4.1.2 Shrinking hole colloidal lithography . . . 18
4.2 Characterisation . . . 19
4.2.1 Reactor . . . 19
4.2.2 Scanning Electron Microscope . . . 22
4.2.3 X-ray Photoelectron Spectroscopy . . . 22
4.3 Computation . . . 23

5 Results **25**
5.1 Direct sensing . . . 25
5.1.1 Temperature programmed oxidation and reduction of copper nanoparticles . . . 25
5.1.1.1 Reversibility of oxidation and reduction processes . . . 27
5.1.2 Temperature programmed oxidation and reduction of cobalt nanoparticles . . . 31
5.2 MLWA model computation . . . 44
5.2.1 Copper . . . 44

5.2.2 Cobalt 48
5.3 Indirect plasmonic sensing 50

6 Conclusions and outlook **53**
6.1 Oxidation and reduction properties of cobalt and copper 53
6.1.1 Copper 53
6.1.2 Cobalt 54
6.1.3 Indirect sensing 54
6.2 Outlook 54
6.2.1 Mass spectrometry 55
6.2.2 Sintering 55
6.2.3 Simulation 55

Bibliography **56**

A Appendix 1 **I**
A.1 Temperature-programmed oxidation and reduction of copper nanoparticles I
A.2 Temperature-programmed oxidation and reduction of cobalt nanoparticles I
A.3 Temperature-programmed oxidation and reduction of cobalt film . . . VI
A.4 Temperature ramps of Co film in Ar VII

1
Introduction

The field of catalysis is well established and industrially widely applied. Catalysts mediate activation barriers in chemical processes and thus offer possibilities to reduce the cost and time of production of chemicals, as well as provide control over reaction selectivity. To derive fundamental understanding of catalytic process in order to optimize them the field has thus been in the focus of both the industry and academic research for a long time. One of the fundamental properties of many catalytic reactions are the oxidation and reduction behaviour, which are accompanied by changes in the electronic as well as crystalline structure of the catalyst and, consequently, its performance. In this field, there is a need for instruments that in an accurate and efficient way can characterize catalytic processes and materials, and predict what changes of the involved materials that control the overall efficiency and selectivity. Today there are various kinds of characterisation methods for the nanoscale analysis of catalyst materials, where XANES, XPS and XRD are examples based on X-ray radiation. Other methods such as SEM and TEM use electron as probes for imaging and various types of electron-based spectroscopies such as EELS and diffraction. Various of these methods are however, applicable only in a limited fashion in terms of, for example pressure, when in situ measurements are of interest. They are also very expensive in terms of required hardware and time consuming to work with. Hence there is a need to find new efficient "bench top" methods as a compliment to the established ones.

During the past years the area of application of surface plasmons has attracted a lot of attention, as illustrated in Figure 1.1, where the number of articles published annually containing the phrase "surface plasmon" is presented. The optical properties of plasmonic materials and nanoparticles have generated a lot of applications, for example, in the field of cancer treatment [2], solar cells [3] and spectroscopy [4], to just mention a few. In the application of detection and sensing most focus has been on the noble metals gold and silver, due to their strong abilities to generate plasmonic resonance with low losses. This area of research has, however, been expanded the last years to include other metals, such as aluminium, platinum, palladium, copper and nickel.

In this master thesis work the transition metals copper and cobalt in their nanoparticulate form have been investigated in different environments of hydrogen and oxygen, to enable in situ correlation of the optical change of the material with their different oxidation states.

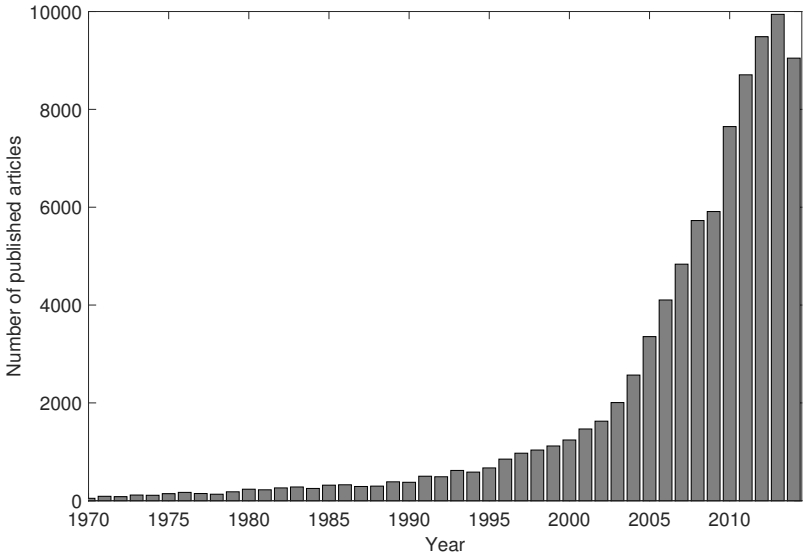

Figure 1.1: The growth of the field "plasmonics". The figure shows the number of scientific articles published annually containing the phrase "surface plasmon". The data is provided by the Chalmers University library database.

1.1 Purpose of the project

This master thesis project aims at demonstrating how plasmonic sensing can be used to detect oxidation and reduction processes in nanoparticles in situ. The hypothesis of the project is that the different oxidation states of particles will change the optical properties in such an extent that the respective transitions are detectable by plasmonic sensing.

The project is primarily an experimental work where the oxidation and reduction process of the transition metals copper and cobalt will be investigated. The two metals are of great importance in a lot of catalytic applications, for example methanol synthesis, respectively the Fischer-Tropsch process. In the field of plasmonics, copper is the most studied of the two metals, but mainly in the field of enhancing catalysts reactions, not as a characterising instrument. Cobalt has yet not received much of interest in fundamental plasmonics research, probably due to its weak plasmonic response.

The overall goal of this project is to establish experimental strategies to detect the transition between different oxidation states of cobalt and copper nanoparticles in situ, by correlating the corresponding changes in optical (plasmonic) response with the environmental change in terms of temperature in oxidizing or reducing atmosphere. The study will thus deepen the knowledge about oxidation and reduction processes of nanoparticles, and contribute to finding new ways of detecting these reactions in situ.

2

Plasmonic resonance

An elementary property of the electromagnetic radiation is the ability to interact with charged particles by the electromagnetic force, one of the four fundamental interaction forces in our universe. To describe this interaction with electrons the classical Lorentz model can be used. There we treat the particles as independent harmonic oscillators [5]. When the electrons are exposed to a local electric field $\mathbf{E}$ the equation of motion can be described as

$$m_e \left(\frac{\partial^2 \mathbf{x}}{\partial t^2} + \xi \frac{\partial \mathbf{x}}{\partial t} \right) + K\mathbf{x} = -e \cdot \mathbf{E} \tag{2.1}$$

where m_e is the mass of the electron, $\mathbf{x}$ is the displacement from equilibrium, ξ is the damping constant, K the spring constant and e is the elemental charge. The solution of Equation 2.1 reads

$$\mathbf{x} = \frac{e/m_e}{\omega_0^2 - \omega^2 - i\xi\omega} \tag{2.2}$$

where $\omega_0 = \sqrt{K/m_e}$ is the resonance frequency of the oscillator.
For a system of separated positive and negative charges the electric dipole moment, $\mathbf{p}$, is a measure of the separation of these two. The dipole moment is defined as the charge displacement times the electron charge

$$\mathbf{p} = -e\mathbf{x} = \frac{e^2/m_e}{\omega_0^2 - \omega^2 - i\xi\omega}\mathbf{E} \tag{2.3}$$

The material polarization (dipole momentum per unit volume) is given by

$$\mathbf{P} = N\mathbf{p} = \frac{\omega_p^2}{\omega_0^2 - \omega^2 - i\xi\omega}\varepsilon_0\mathbf{E} \tag{2.4}$$

where ε_0 is the permittivity of vacuum and N is the electron density and

$$\omega_p = \sqrt{\frac{Ne^2}{m_e\varepsilon_0}} \tag{2.5}$$

is the plasma frequency. To account for the non-independent relation between electrons, often the effective electron mass is used instead of the free electron mass, m_e. The oscillation frequency depends on the density of electrons, the effective mass, and the shape and size of charge distribution [6].

Equation 2.4 can be rewritten to include the complex dielectric function, ε,

$$\varepsilon(\omega) = 1 + \frac{\omega_p^2}{\omega_0^2 - \omega^2 - i\xi\omega} \tag{2.6}$$

such as that the polarizability can be written on the constitutive form

$$\mathbf{P} = \varepsilon_0(\varepsilon - 1)\mathbf{E} \tag{2.7}$$

Due to the Drude model, which predicts that the microscopic behaviour of the electrons can be treated with classical physical rules, we can set $K = 0$, which makes ω_0 vanish. The complex dielectric function will take form as

$$\varepsilon(\omega) = 1 - \frac{\omega_p^2}{\omega^2 + \xi^2} + i\frac{\omega_p^2\xi}{\omega(\omega^2 + \xi^2)} = \varepsilon_r + i\varepsilon_i \tag{2.8}$$

where ε_r and ε_i are the real respectively the imaginary parts of the complex dielectric function. ε can be related to the refractive index, n, and the extinction coefficient k by

$$\varepsilon = (n^2 - k^2) + i2nk \tag{2.9}$$

In room temperature conditions most metals have a very low value of ξ, which implies that that the real part of the dielectric function will be close to 0 when $\omega = \omega_p$[5]. In this case, when an external field is applied, the free electrons will move collectively and build a displacement charge. The created internal electric field will force the displacement to restore the initial electrical distribution, due to the Coulomb attraction between the electrons and the nuclei. This collective motion of electrons is called bulk plasmon resonance, where plasmons are the corresponding quasi-particles with energy $\hbar\omega_p$.

2.1 Surface plasmons

The behaviour of the electrons at the surface is somewhat different from the bulk. The plane parallel mobility of electrons at the surface is high but the interface between the surface and the surrounding medium limits the normal direction mobility. The surface plasmon resonance (SPR) frequency, ω_{SPR} is, for positive values of refractive index, reduced according to equation 2.10 [7]

$$\omega_{SPR} = \frac{\omega_p}{\sqrt{1+n}} \tag{2.10}$$

2.2 Localized surface plasmons

For metal particles whose size is in the quasi-static regime, where the size of the particle is smaller than the incoming wavelength of the light, all the free electrons in the particle will be collectively excited. This phenomenon is called localized surface

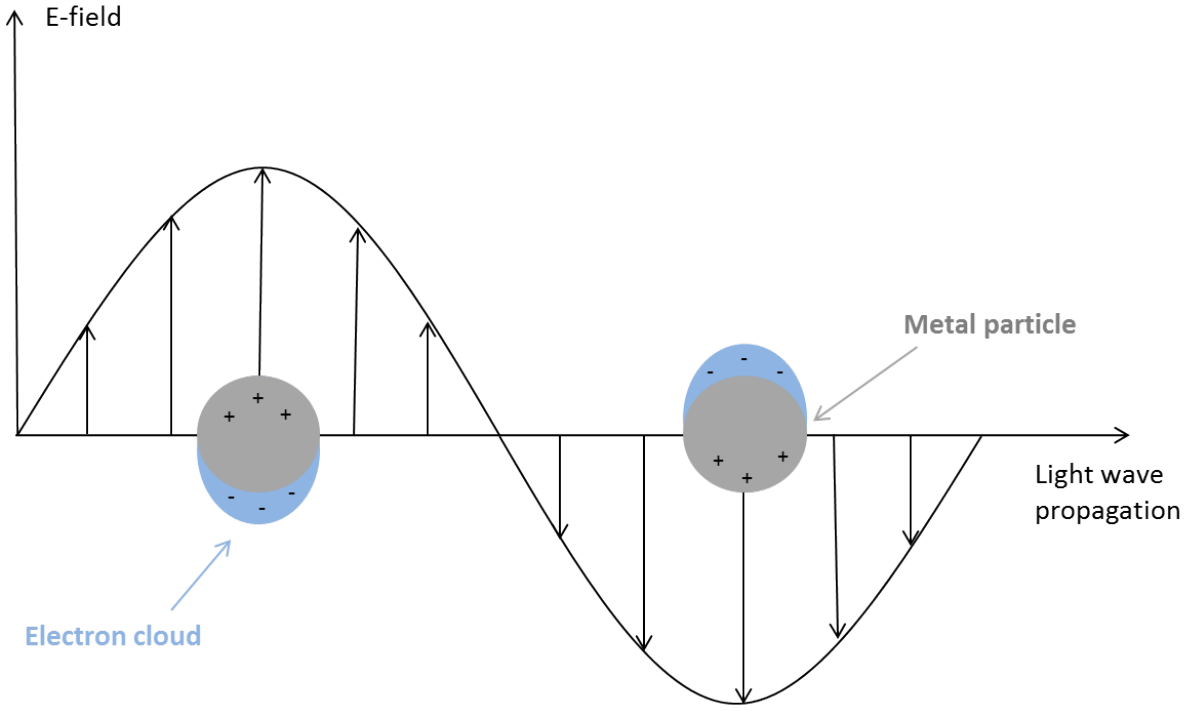

Figure 2.1: The electric dipole movement when an electrical field is applied on nanoparticles of size smaller than the wavelength, λ.

plasmon resonance (LSPR). For these types of small particles we can assume the oscillation as a point electric dipole. The dipole moment of the induced dipole can be considered as

$$\mathbf{P} = \varepsilon_d \alpha(\omega)\mathbf{E} \tag{2.11}$$

where ε_d is the dielectric constant of the surrounding dielectric and

$$\alpha(\omega) = 4\pi\varepsilon_0 a^3 \frac{\varepsilon_m - \varepsilon_d}{\varepsilon_m + 2\varepsilon_d} \tag{2.12}$$

is the dipole polarizability of the sphere. ε_m is the complex dielectric function of the sphere material and a is the radius of the particle [8]. When the denominator of the polarizability goes to zero it diverges, which implies a resonance. From Equation 2.12 we see that this occurs when

$$\mid \varepsilon_m(\omega) + 2\varepsilon_d \mid \rightarrow 0 \tag{2.13}$$

$$\Rightarrow \mid \varepsilon_{m,r}(\omega) + 2\varepsilon_d \mid^2 + \mid \varepsilon_{m,i}(\omega) \mid^2 \rightarrow 0 \tag{2.14}$$

A large polarizability is therefore achieved when the imaginary part $\varepsilon_{m,i}$ goes to zero and the real part $\varepsilon_{m,r}$ is equal to $-2\varepsilon_d$. If the expression for a Drude-dielectric function, Equation 2.6, is inserted into Equation 2.12 the dipole polarizability of the sphere is [5]

$$\alpha(\omega) = 4\pi\varepsilon_0 a^3 \frac{\omega_{LSPR}^2}{\omega_{LSPR}^2 - \omega^2 - i\xi\omega} \tag{2.15}$$

where the localized surface plasmon resonance frequency, ω_{LSPR}, can be calculated from Equation 2.16.

$$\omega_{LSPR} = \frac{\omega_p}{\sqrt{1 + 2\varepsilon_d}} = \sqrt{\frac{Ne^2}{m_e\varepsilon_0(1 + 2\varepsilon_d)}} \tag{2.16}$$

The complex permittivity, ε, represents the relationship between the electric and magnetic fields in a material. The imaginary part is directly related to the resistivity, while the real part tells you whether the material has a capacitative or inductive optical response. The ratio between the two corresponds to the phase lag between electric and magnetic fields.

2.3 Decay of LSPR

The lifetime, τ, of a plasmonic excitation in a nanoparticle is typically about a few femtoseconds [9]. The exact value depends on the kind of material, and the size, shape and dielectric environment of the particle. The mechanism of the decay occurs radiatively, by photon emission due to the elastic light scattering, or non-radiatively, also called absorption. The latter mechanism stems from electron-hole pair formation due to intra- and interband excitations and is called Landau damping. Landau damping is inverse proportional to the particle size, which makes it the dominating decay mechanism of small particles [10]. It has been shown that the radiative damping is increasing with the particle size [11]. The lifetime can mathematically be described as [9]

$$\tau = \frac{h}{\Gamma_{LSPR}} \tag{2.17}$$

where h is the Planck constant and Γ_{LSPR} is the spectral linewidth.

2.4 Application of plasmonics

The applications of "plasmonics" are spread over a lot of different areas. The first documented use is the famous Lycurgus cup from the 4th-century. The Romans discovered that the dichroic glass material changed its colour depending on if the light was reflected or transmitted from the cup, which displays spectacular optical effects. What was not known then, but discovered today, was that the effect was a cause of the 50-100 nm small colloidal gold and silver nanoparticles in the material. In modern time the plasmonic properties has been further developed in the areas of solar cells, optical transistors, and chemical and biological sensors to mention a few. In this thesis the application of plasmonic nanoparticles is based within sensing.

2.5 Optical characterization

When a material is irradiated with light two main things will occur. Parts of the light will be scattered and parts of it will be absorbed. For the specific case of the plasmonic excitations they will after interaction with light either decay by radiation (scattering) or by electron-hole pair excitations (absorption). The first mechanism, radiation, originates from the elastic scattering of electromagnetic energy by the induced dipole. The electron-hole pair excitation relaxes via an electron-hole pair cascade and, eventually, via electron-phonon coupling, which induces heat. These two different mechanisms of decay can be measured in the far field and are characterized by their corresponding cross-section, σ, which expresses the likelihood of interaction between the photons and the nanoparticle via the specific decay process. In Equation 2.18 and 2.19 the expressions for the crossections of absorption, σ_{abs}, and the scattering, σ_{sca}, are given.

$$\sigma_{abs} = k\mathrm{Im}\{\alpha(\omega)\} = 4\pi\varepsilon_0 k a^3 \mathrm{Im}\{\frac{\omega_{LSPR}^2}{\omega_{LSPR}^2 - \omega^2 - i\xi\omega}\} \tag{2.18}$$

$$\sigma_{sca} = \frac{k^4}{6\pi}|\alpha(\omega)|^2 = \frac{8k^4\varepsilon_0^2 a^6}{3}\left|\frac{\omega_{LSPR}^2}{\omega_{LSPR}^2 - \omega^2 - i\xi\omega}\right|^2 \tag{2.19}$$

where $k = \frac{2\pi}{\lambda}$ is the wave vector. The sum of the absorption and scattering is called extinction

$$\sigma_{ext} = \sigma_{abs} + \sigma_{sca} \tag{2.20}$$

According to Equations 2.18 and 2.19 the absorption is proportional to the particle volume (a^3) and the scattering is proportional to the square of the volume (a^6). For very small particles, the absorption will therefore dominate, which has been experimentally proved by Zorić et al. [12]. For large particles the scattering will dominate, which broadens the spectra via radiation damping.

The absorption of light can be calculated from Equation 2.21

$$A = -log\left(\frac{I}{I_0}\right) \tag{2.21}$$

where I_0 is the intensity of the incident light and I is the measured transmitted intensity. Sometimes we refer to the transmittance T by

$$T = \frac{I}{I_0} \tag{2.22}$$

The ability of gold and silver to exhibit strong SPR in the visible light-range makes them well used as plasmonic sensors. Gold has also the intrinsic ability of being more stable for oxidation processes. In the past years copper has also been studied frequently and seems to generate plasmonic response in an extent comparable to gold and silver [13].

Comparing different plasmonic resonances

There are various ways of comparing different materials in their ability to interact with light. A common way to describe plasmonic resonance behaviour is to calculate the extinction efficiency, Q_{ext}. It is the ratio between the cross section of extinction and the geometrical area of the particle [12] according to Equation 2.23

$$Q_{ext} = \frac{\sigma_{ext}}{A} \tag{2.23}$$

According to Equation 2.16 the frequency, which also embraces the wavelength, where the plasmonic resonance occurs, is dependent on the dielectric function, ε, of the plasmonic material itself and of its surrounding medium. The dielectric function, as a descriptor of a material property or "state" (e.g. oxidation) is itself changing when the environment hosting the material is changing, such as temperature and chemical composition. By tracking and analyzing how a change in the extinction spectra of a plasmonic material corresponds with a certain process induced by a change in its surrounding, plasmonic nanoparticles can be used as a detection tool for this change, for example, by measuring how the extinction of the light is changing over time. The technique has an advantage of being short distance sensitive, which is due to the small sensing volume, an effect of the enhanced electric field around the particle. The field is very rapidly decaying away from the surface of the plasmon induced particle. The field typically stretch only a few nanometers away from the particle before it is undetectable. The sensing volume of the particles can, however, be tuned by changing the form of the structures.

2.5.1 Direct and indirect nanoplasmonic sensing

An efficient way to use plasmonic sensors is to use the investigated material itself as a sensor. This is called direct plasmonic sensing and the technique is straightforward but is limited to materials with ability to support plasmonic resonance themselves. The output signal will also be very low if the particles are small, which decreases the signal to noise ratio.

To enable studies of other materials where the plasmonic response is low Langhammer et al. invented the indirect plasmonic sensing (INPS) approach in 2010 [4]. The sensor consist of an antenna of a material with high plasmonic response ability, often Au, and the analyzed material is placed in close proximity to the sensor. A thin dielectric layer, often SiO_2, is in some cases covering the antenna particle to ensure that the antenna particle it self does not change its properties. The technique makes it possible to study smaller structures, down to 1 nm [14], and the choice of materials expands to non-metallic. An illustration of the difference between direct and indirect plasmonic sensing, when detecting the same size of particles, is given in Figure 2.2.

For different polarised light directions the plasmons can be induced in- or outline of the indirect sensing structure. For the light polarized outline of the structure the signal will be a sum of the two antenna particle and the particle of interest. If the

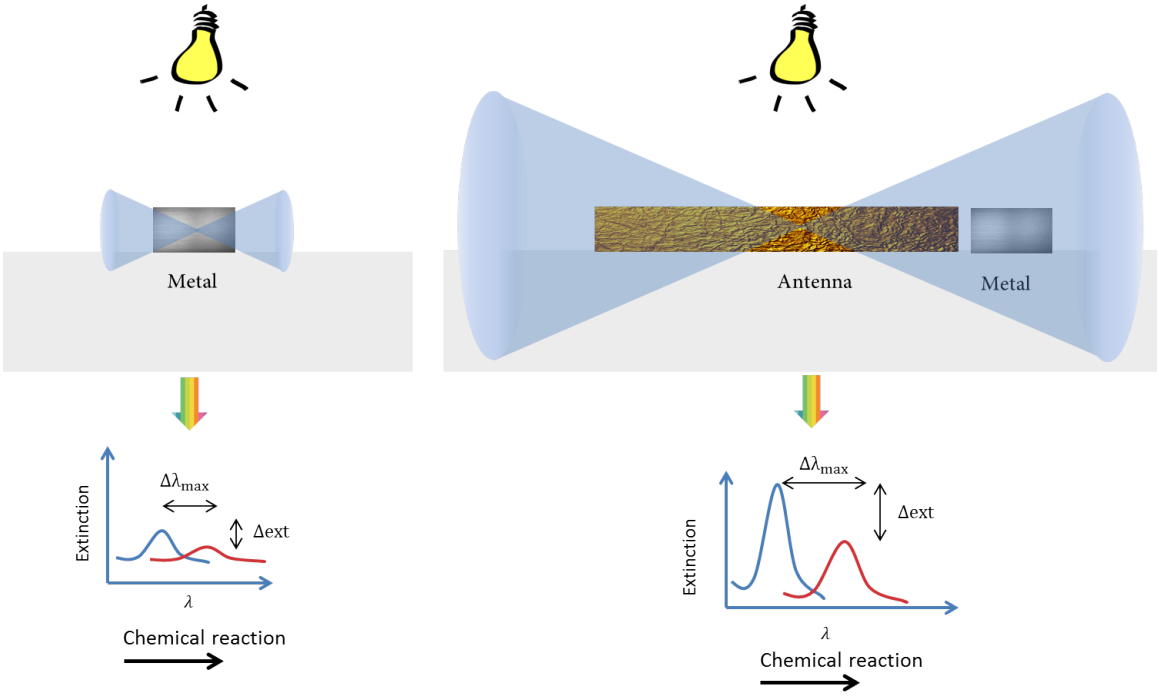

Figure 2.2: Illustration of the direct (left) and indirect (right) plasmonic sensing. The light interacts with the samples and the extinction is measured. When the dielectric function of the samples change, due to external influence, extinction peak will shift from the initial state (blue colour) to the final state (red colour). In the indirect sensing sample the extinction peak is higher and narrower due to the usage of a plasmonic material and the much larger size of the plasmonic antenna.

latter one is small and of a material with low plasmonic response the contribution of this one will be very small. We will in other words mainly see the antenna plasmon peak. For the other polarized direction, inline with the structue, the electrical field of the detected particle will affect the antenna, which will change the plasmonic resonance response. By placing the particle in the most favourable position in relation to the antenna, called hot spot, the enhanced field will be the greatest and the signal will be high. By subtracting the optical signals from the two polarized light directions, the signal that origin from the detected particle can be determined. The first application of INPS was to probe the metal-hydride formation process of palladium nanodisks [14], where the technique has pushed the knowledge of hydrogen storage sensing forward.

3

Heterogeneous catalysis

The usage of catalysis spans over a large spectrum of industrial processes where ammonia production, cracking of oil products, and mitigation of air pollutants, as for example in the three-way catalyst of a car, are some of the examples. Catalysis is used in more than 90 % of the chemical industries, to reduce both the cost and increase the production rate of a wanted product. Its importance in such a wide field of disciplines has attracted the research in order to understand the underlying properties of the catalytic materials as a means to further improve them.

3.1 Catalysis

During a chemical reaction bonds between the atoms in a reactant molecule are broken and new bonds formed in the product. To enable a spontaneous reaction between two molecules from a thermodynamics point of view, the final state must be of a lower total Gibbs free energy than the initial one. However, even if a reaction is thermodynamically downhill, most chemical reactions still do not occur spontaneously because they are kinetically hindered, i.e. an energy barrier, the activation energy (E_a), has to be overcome in order to start the reaction.

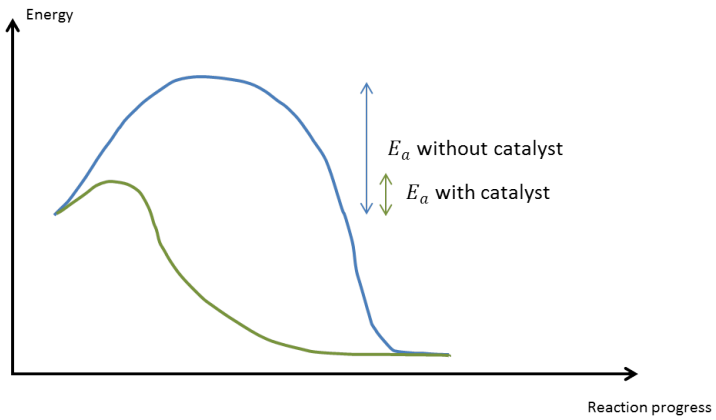

Figure 3.1: Illustration of the effect of a catalyst to the reaction procedure. The presence of the catalyst, green line, decrease the activation barrier comparing to the uncatalysed reaction, blue line. The final energy state is the same in the two cases.

Catalysis can be divided into three main groups, *homogeneous catalysis* where the reacting species and the catalyst are in the same phase, *biocatalysis* where the catalyst is an enzyme, and *heterogeneous catalysis* where the reacting species and the

catalyst are in different phases. In the industrial usage of catalysis the latter one is dominating with 80 % of all applications [15].

The role of the catalyst is often both to act as a surface for reactions to occur, which is the case for heterogeneous catalysis, and to form temporary bonds with the reactants. For reactions where oxidation and reductions take place (redox reactions) the transition metals are the most used ones, due to their ability to exist in different oxidation states. This is the case since their unfilled d-orbital electrons enable them to accept electrons, which is a necessary mechanism to enable the reactions to take place [16].

The oxidation state of an atom is an approximation of what sign and absolute value the charge of a certain atom should be if it would be an ion. This value depends on the number of unpaired valence electrons, which can be seen in the electron configuration of the elements. For most of the transition metals the highest possible oxidation state is the sum of the unpaired d-electrons plus the two s-orbital electrons. This rule is however not applicable for Cu. The electron configuration of Cu is $[Ar]4s^1 3d^{10}$, and the primary formed oxides are Cu(I) and Cu(II).

For bulk metals their oxidation is controlled by diffusion of electrons and ions, under influence of the gradients from the generated electric field, respectively the concentration. For nanoparticles, the electric field, induced by the free electron movement, is the dominating driving force of oxidation. The area of oxidising nanoparticles is not as well-studied as it is for bulk materials. When a metal oxidises, it will in most cases be converted into a semiconductor or insulator. The material will thereby also change its optical properties. For a semiconductor, for example, a characteristic band gap will arise.

3.2 Nanoparticles

Nanoparticles can exhibit completely different properties compared to the corresponding bulk material. Their small sizes brings along, relative to atoms in the the bulk, larger amounts of surface and interface atoms. The material will also change its electronic properties when reaching the nano level, due to discretization of energy states in the sub 5 nm size regime. Their large specific surface area makes nanoparticles highly desirable for catalysis, especially where the catalytic material is expensive and the amount of used material requires to be decreased.

Some properties do have a specially strong relation to the size of the particles. It has, for example, been shown that the generation of electron-hole pairs, which is a specially eager feature in photocatalysis, requires particles smaller than 20 nm [17].

3.3 Materials used in this study and their key propertis

In this study the two transition metals copper (Cu) and cobalt (Co) has been studied during different redox circumstances using direct plasmonic sensing.

3.3.1 Cu

Copper, abbreviated Cu, is a transition metal with atomic number 29 in the periodic table. It shares the same group as silver and gold, in the coinage metal group, due to their use as payment medium. They all share the property of high conductivity of both heat and electricity. Copper is, however, not as noble as Ag and Au and thus, much more likely to oxidise. The application of copper nanoparticles in heterogeneous catalysis has during the past years been an area of great interest. For example, it has been found that copper particles can catalyze methanol synthesis [21], increase the hydrogen production in the water-gas-shift reaction[22] and reduce carbon dioxide to hydrocarbons in photocatalytic reduction processes [23]. The application of Cu also includes the areas of photovoltaics and optics. Its ability to support LSPR in the visible light range makes it to a candidate of replacing gold and silver as plasmonic usable material.

When copper is exposed to oxygen it can form different kind of metal oxides. The most common existing ones are CuO, *cupric oxide*, and Cu_2O, *cuprous oxide*. The colours of the oxides are black respectively red and they are, together with copper hydroxide and copper carbonate, forming the characterising green shell colour at copper surfaces when they are exposed to air [24], [25]. It is of great interest to investigate the role of Cu and its oxides, for example in electrical circuits where an oxide layer decreases the conductivity dramatically.

According to Tanaka et al. copper nanoparticles of size 20 nm should be fully oxidised at a temperature of 190-200°C when exposed to 20 % O_2 gas in an inert carrier gas [26]. The same authors also showed that the type of formed copper oxide was strongly dependent on if the temperature was below or above this threshold value of 200°C, see Figure 3.2.
When the copper nanoparticles are at a temperature lower than threshold temperature the particles will form a thick Cu_2O core and a thin CuO shell. If the temperature rises, the CuO shell will increase and the Cu_2O core decrease. The oxidation behaviour of copper surface films in air environment has been investigated by Poling in 1969. The conclusions was that the metal formed Cu_2O at 140°C. For temperatures above 200°C CuO started to grow on top of Cu_2O [27].

For metallic Cu, the interband absorption position is around 500 nm. In this spectral area the plasmonic excitation is likely to decay via coupling to these allowed interband excitations and thus gets significantly damped. Specifically, it has also been shown that an overlap of interband transition and a plasmon resonance results in a double peak structure [28]. The LSPR peak position of copper is inverse

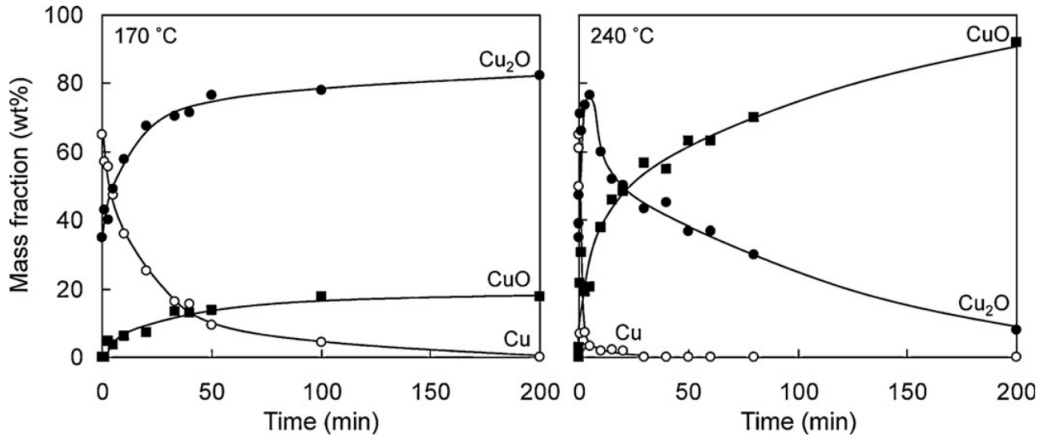

Figure 3.2: Mass fraction of copper and its oxides CuO and Cu_2O during oxidation of a copper nanoparticles (20 nm) as a function of time, for 170°C (left) and 240°C (right) [26].

proportional to the energy of the light, which means that an increase of size of the particles will red-shift the position of spectra. This conclusion has been confirmed both by experiments and DDA simulations [13].

3.3.2 Co

Cobalt (Co) is a transition metal with atomic number 27 in the periodic table, in the same group as rhodium (Rh), iridium (Ir) and meitnerium (Mt). Cobalt is, due to its unpaired electrons, a ferro-magnetic material at room temperature. This means that it creates parallel magnetic moments when a magnetic field is aligned, which induces the magnetic property of the metal. The most common applications of Co are in combination with other materials, often with metals in alloys. Beside of its use in permanent magnets the metal can be used to improve the temperature stability and prohibit corrosion in, for example, steels.

Cobalt is also an important part in carbon monoxide conversion reactions, such as the Fischer-Tropsch process. In the Fischer Tropsch process carbon monoxide, which is a toxic and environmental dangerous gas, reacts with hydrogen to form long-chain hydrocarbons, which, for example, can be used as fuels [29] or raw materials for fine chemicals.

$$\mathrm{CO} + \frac{1}{2}\mathrm{H_2} \xrightarrow{\mathrm{Co}} \mathrm{C}_x\mathrm{H}_y + \mathrm{H_2O} \tag{3.1}$$

This ability is of specially interest in remote locations where the access of energy is limited [30]. Cobalt catalyst nanoparticles of the size 3-20 nm are very promising for their high quality conversion in this process, thanks to its high activity and selectivity toward the wanted reaction [29]. There is, however, also a couple of catalyst deactivation mechanisms that decrease the performance. One of them is sintering, wherein the particles merge into bigger ones which reduce the total surface area

of the catalyst and thus its overall activity. It has been found that an oxidation-reduction process might regenerate sintered cobalt particles, by the Kirkendall effect [31].

When cobalt is exposed to oxygen mainly two oxides will be formed: CoO and Co_3O_4. The reduction process will occur in two steps. The first reduction of Co_3O_4 to CoO occur fast at temperatures above 300°C:

$$Co_3O_4 + H_2 \rightarrow 3CoO + H_2O \tag{3.2}$$

and later at 400°C the next reduction reaction occur, with a much lower reaction rate [32]:

$$CoO + H_2 \rightarrow Co + H_2O \tag{3.3}$$

4
Methods

In this chapter the methodology of the experiments is described. The chapter is divided into the sections Fabrication, Characterisation and Computation.

4.1 Fabrication

4.1.1 Hole-mask colloidal lithography

The fabrication of the arrays of the nanoparticles of different sizes used in this project has the latest years been possible, thanks to the revolutionizing method Hole-mask Colloidal Lithography (HCL). In contrast to the previous top-down methods, HCL provides a bottom-up nanofabrication method, where the use of materials, size and forms spans over a rich variety [33]. The procedure of HCL that was used in this project can be summarized in the following steps:

1. Cleaning the substrate by sonication, first in acetone, then in iso-propanole and last in water. Each for 3 min.

2. Spin coating of poly(methyl methacrylate) (PMMA) for 1 minute and soft baking in 10 minutes at 170°C.

3. A short (5 s) oxygen plasma etching, to increase the hydrophilicity of the surface.

4. Adding polyelectrolyte monolayer polydiallyldimethylammonium (PDDA) to the substrate surface for 40 seconds, where after rinsing in de-ionized water for 20 seconds to remove the excess PDDA. The substrate is thereafter dried in a clean N_2 flow. This step forms a thin charged adhesive layer on the polymer surface.

5. Adding of an oppositely charged solution to the PDDA, containing colloidal polystyrene (PS) to the substrate during 3 min, where after water rinsing in 20 seconds.

6. 20 nm Cr deposition in an evaporator.

7. By using tape the polystyrene particles are stripped away, which creates holes in the Cr film layer. The size of polystyrene determines the spacing and diameter of the holes.

8. Oxygen plasma etching of sample, which will create a partial undercut in the PMMA layer in the exposed regions of the holes in the Cr masks. The depth of the undercut can be controlled very precisely, by adjusting the etching time. In this report a etching time of 5 minutes has been used.

9. Metal evaporation to form the nanoparticles on the surface.

10. Lift-off in acetone and low power sonication.

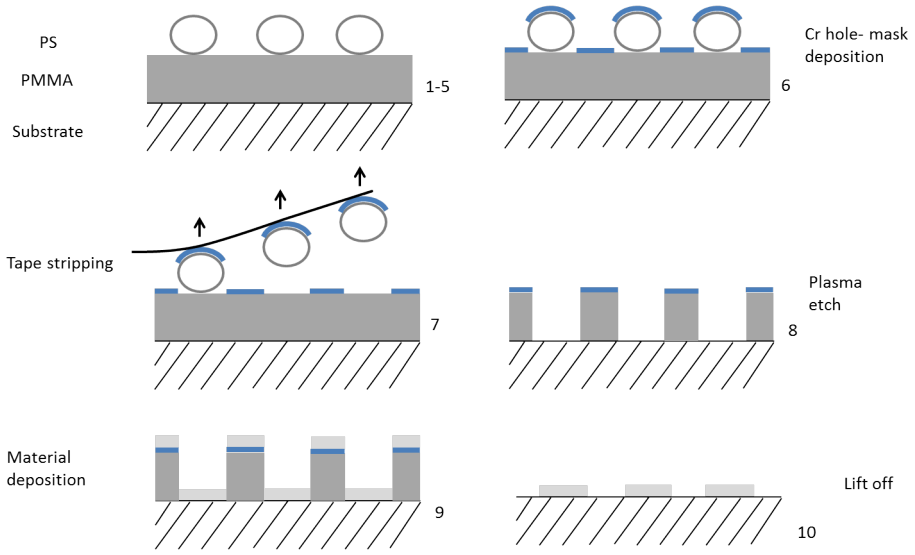

Figure 4.1: Illustration of the hole-colloidal lithography process.

4.1.2 Shrinking hole colloidal lithography

Since the method HCL was invented in 2007 improvements has been done. With the Shrinking hole colloidal lithography (SHCL) [34] method the accuracy and flexibility has been improved and it enables to deposit several metals, with different sizes. In this article the direct plasmonic sensing samples were fabricated with HCL and those of indirect plasmonic sensing type were fabricated with SHCL.

In the SHCL method the materials are deposited with certain angles through the holes in the Cr mask produced by the first steps of standard HCL. This will make the hole successively shrink its size through deposition of material on the rim, which makes it possible to control the size and position of each nanoparticle grown on the support very accurately. Between the two separate deposition steps chromium can be deposited in order to shrink the hole, which makes it possible to restrict the used first kind of deposited material. In the early study of this structure a chromium etch solution was used to dissolve the chromium after the final structure was done. Copper, which was used in this thesis, is however not able to sustain this Cr-etch solution, which enforces other kind of strategies.

In this work the INPS structure with copper was therefore done using the so called "funnel approach", which implies that the chromium is deposited with such a high angle so that it only grows on the wall of the PMMA layer in the hole of the mask, see Figure 4.2. This make it possible to shrink the hole, but avoid Cr deposition on the INPS structure.

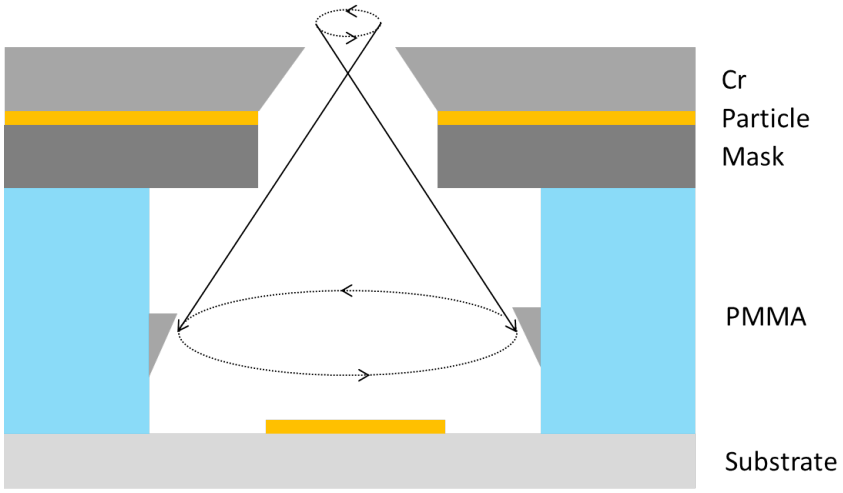

Figure 4.2: Illustrative description of the funneling approach. Chromium is deposited on the walls of the PMMA, and shrinks the hole.

4.2 Characterisation

4.2.1 Reactor

To investigate the oxidation and reduction behaviour of cobalt and copper particles in situ using nanoplasmonic sensing, a quartz tube flow reactor called Insplorion X1 was used. Inside the reactor a heating coil and a thermocouple was attached, to heat respectively measure the temperature of the sample. Two optical fiber cables were attached perpendicular to the reactor, illuminating and collecting light through the quartz tube and the sample, see Figure 4.3.

In the first part of the project HCL-fabricated arrays of Cu or Co nanoparticles (direct sensing approach) were exposed to linear temperature ramps in controlled concentrations of H_2/O_2 in inert Ar carrier gas. The temperature was increasing with a constant rate (5°C/min) for all the experiments. In Figure 4.4 a schematic picture of the reactor experiment is given.

For the direct sensing samples both Cu and Co were tested, in different sizes. For the indirect sensing approach only Cu was tested as reacting particle, with gold particles as antenna. The three different sample setups are illustrated in Figure 4.5. To enable a study of the copper contribution to the extinction spectrum of the indirect sensing samples, a beam splitter was attached to the collecting light fiber, whereas

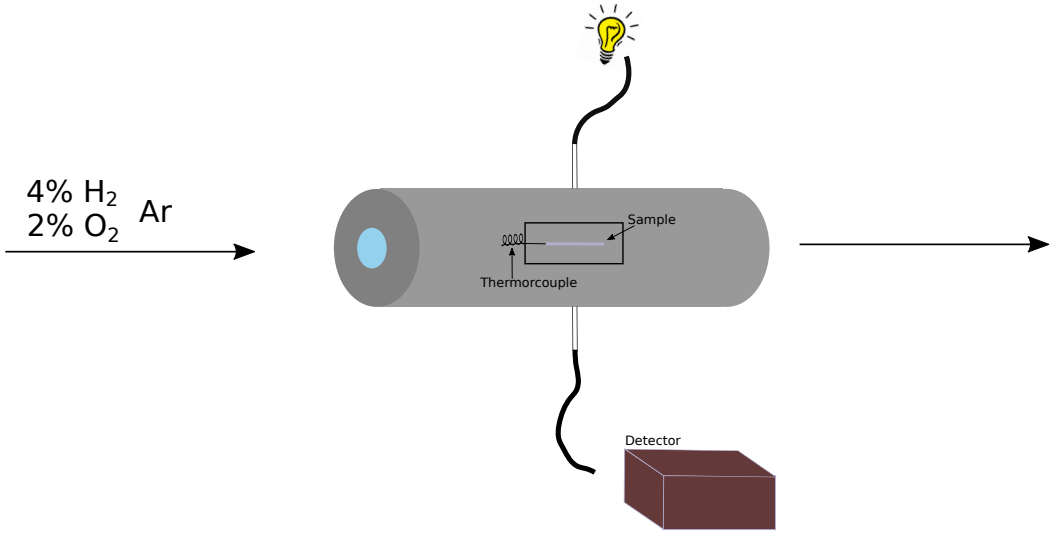

Figure 4.3: Schematic picture of the Insplorion X1 reactor setup. It consist of an insulated quartz tube where the gas can flow from the one side to the other and light can be transmitted through the sample holder. The temperature is controlled by a heating coil and measured by a thermocouple, connected to the sample holder.

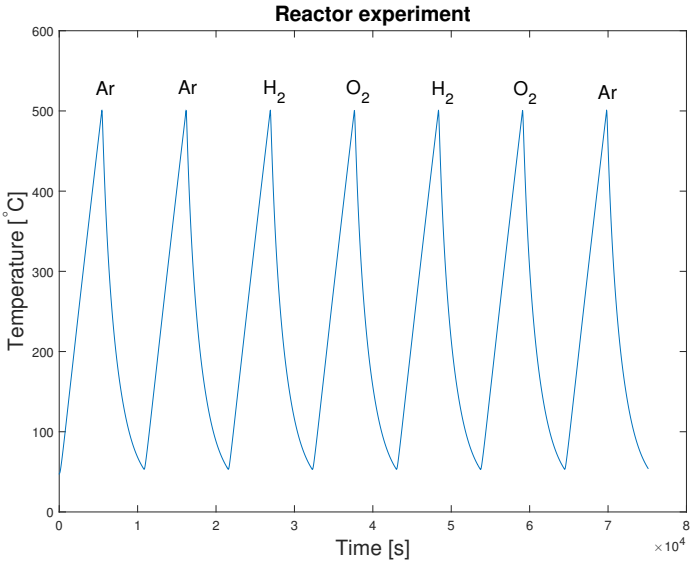

Figure 4.4: Schematic depiction of a typical reactor experiment sequence of temperature ramps in different gas environments. The maximum temperatures and the use of gases were different for different experiments.

two fibers was connected to the collector and measured each polarized light direction separately. The polarized direction outline of the structure measures the contribution of plasmonic resonance from each structure themselves and the polarized light inline with the structure measures the coupling of the localized plasmonic resonance field between the gold antenna and the copper particle. By subtracting the signals

from the two polarized directions, the copper contribution can be determined.

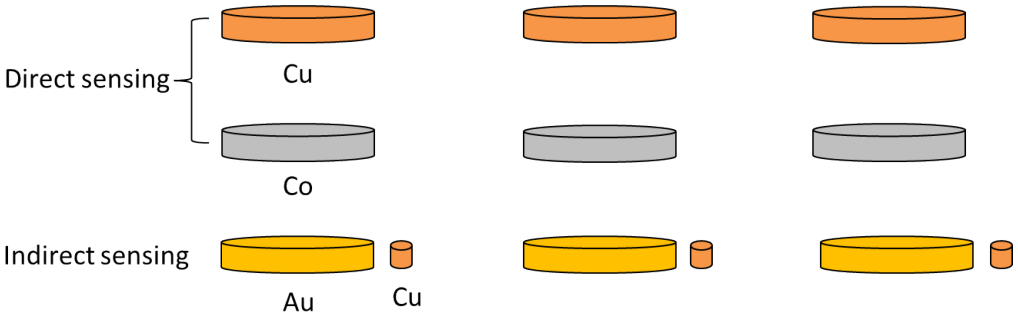

Figure 4.5: Schematic depiction of the three different sample setups.

4.2.2 Scanning Electron Microscope

The scanning electron microscope (SEM) is a modern type of microscope that uses electrons, instead of photons as the ordinary optical microscope does. The wavelength of electrons is much smaller than visible light, which enables a higher resolution of the SEM, down to the nanometer level. In an SEM electrons are emitted from the electron gun towards the sample and the number of backscattered electrons, and secondary electrons, in different directions are detected. The technique is primary used to image the surface structure, but it can also give a significant measure of how the chemical composition changes over the sample. For example, a material with high atomic number has a higher probability to backscatter electrons, which will increase the contrast in the image.

In this project an SEM Zeiss Supra 60 VP has been used for characterizing of the samples.

4.2.3 X-ray Photoelectron Spectroscopy

X-ray photoelectron spectroscopy (XPS) is a spectroscopic technique, measuring the chemical composition of a sample surface. An XPS spectrum is obtained by irradiating a sample with X-rays. When the radiation interacts with the surface it will excite electrons into higher energy states. If the energy of the X-ray photons overcomes the binding energy of the electrons in the material the electrons can escape from the atom into vacuum, provided that they originate from the first few atomic layers. The kinetic energy, E_k, of these electrons can be measured by applying different potentials in an electrical field tunnel. The binding energy, E_b of the electrons is calculated according to Equation 4.1.

$$E_b = h\nu - E_k - \Phi_{sp} \tag{4.1}$$

where $h\nu$ is the energy of the incoming light and Φ_{sp} is the work function of the electron spectrometer. Both $h\nu$ and Φ_{sp} are known from literature for specific materials, and by measuring the kinetic energy of the electrons the binding energy can be calculated and thus a material can be identified.

Not all of the created ions will, however, be in the ground state. There is a probability that the ions will be left in an excited state at a higher energy state than the ground state. If this is the case, the emitted electrons will have a reduced kinetic energy, which will yield so called satellite peaks. All but the s orbital levels gives doublets of possible states of different energies. This is called spin orbit splitting. The area of the peaks have a certain relative ratio between each other that is characteristic for all elements.

4.3 Computation

To enable a comparison between the experimental results obtained from nanoplasmonic sensing and some theoretical considerations a computational study was done. The Cu and Co nanodisks from the experiment were approximated with oblate spheroids, see Figure 4.6, with a core and a shell, which enables a calculation of the dipolar-polarizability in the Modified Long Wavelength Approximation (MLWA) of the electrostatic spheroid theory, according to Equation 4.2 [5].

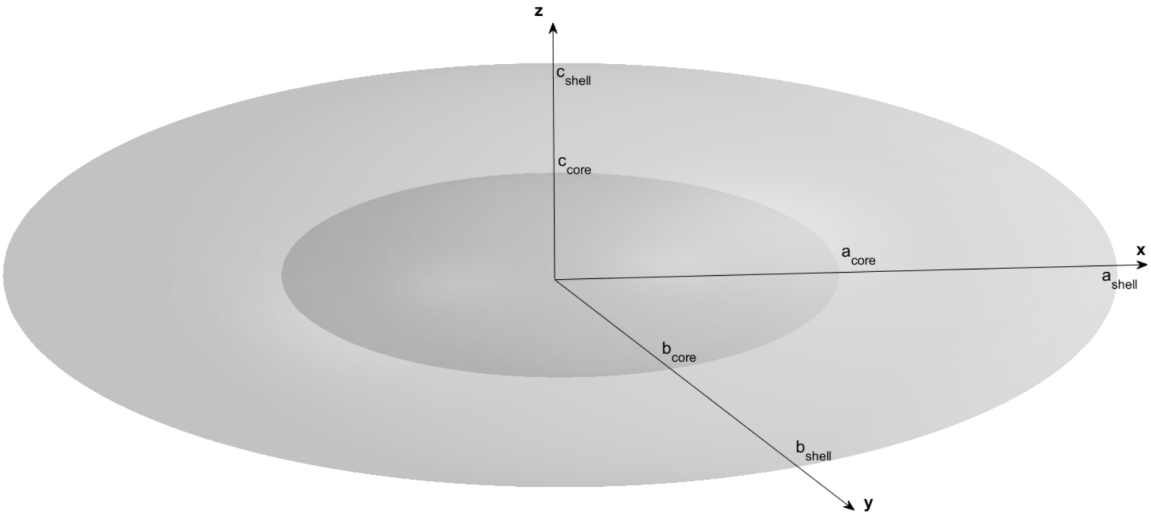

Figure 4.6: Oblate spheroid with inner core

$$\alpha = \frac{v \cdot ((\varepsilon_{shell} - \varepsilon_m) \cdot A + B)}{A \cdot [\varepsilon_m + (\varepsilon_{shell} - \varepsilon_m) L_{shell}] + L_{shell} \cdot B)} \tag{4.2}$$

where

$$A = \varepsilon_{shell} + (\varepsilon_{core} - \varepsilon_{shell})(L_{core} - f L_{shell})$$

$$B = f \varepsilon_{shell} (\varepsilon_{core} - \varepsilon_{shell})$$

and $v = 4\pi a_{shell} b_{shell} c_{shell}/3$ is the volume of the particle, f is the volume fraction of the inner ellipsoid, and L_{shell} and L_{core} are the geometrical factors of the shell and core ellipsoids. In our case the spheroids are oblates, which induce the analytical expression

$$L_i = \frac{g_i}{2e_i^2} \cdot \left[\frac{\pi}{2} - \arctan(g_i)\right] - \frac{g_i^2}{2} \quad i = \text{shell, core} \tag{4.3}$$

where

$$g_i = \left(\frac{1 - e_i^2}{e_i^2}\right)^{1/2} \tag{4.4}$$

and the eccentricity, e_i, of the particle

$$e_i = \sqrt{1 - \frac{c_i^2}{a_i^2}} \tag{4.5}$$

The extinction efficiency (ratio between extinction and projected area of the particle) was calculated from Equation 4.6.

$$Q_{ext} = \left[\pi \cdot (\frac{D}{2})^2\right]^{-1} \cdot \sigma_{ext} = \{\text{When particle size is small}\} = \left[\pi \cdot (\frac{D}{2})^2\right]^{-1} \cdot k\text{Im}\{\alpha(\omega)\} \tag{4.6}$$

To mimic the experiments, a couple of different possible scenarios were calculated using the MLWA model - these were:

Copper
Case 1: Core of metallic Cu and a shell of Cu_2O
Case 2: Core of metallic Cu and a shell of CuO
Case 3: Core of Cu_2O and shell of CuO
Case 4: Core of CuO and shell of Cu_2O

Cobalt
Case 1: Core of metallic Co and a shell of CoO
Case 2: Core of metallic Co and a shell of Co_3O_4
Case 3: Core of CoO and shell of Co_3O_4
Case 4: Core of Co_3O_4 and shell of CoO

This model has its advantages of being rather simple, and the difference between this model and the experiment is both the shape of the particles, where disks here are assumed as spheroids, and the surrounding medium. In the model it is assumed that the particles are covered by a medium with a refractive index of n=1.26, corresponding to an average of glass (n=1.52) and air (n=1). The model do not take the possible volume change into account.

5
Results

In this chapter the results are presented, divided into the sections Direct sensing, MLWA model computation, and Indirect sensing.

5.1 Direct sensing

In this section the results from the in situ temperature-programmed oxidation and reduction flow-reactor experiments on the direct sensing samples are presented. The experiments were done on samples of varying initial average nanoparticle sizes, ranging from 67 nm up to 190 nm. Most of the experiments were done on particles of initial average size 140 nm.

5.1.1 Temperature programmed oxidation and reduction of copper nanoparticles

The temperatures for oxidation (in 2 vol% O_2 in inert Ar) and reduction (in 4 vol% H_2 in inert Ar) of copper nanoparticles were different, where the oxidation required a lower temperature. The temperature range of oxygen exposure was therefore chosen between 50 and 200°C, and for the hydrogen exposure linear temperature cycles between 50 and 400°C were carried out. During the oxidation process the extinction spectrum shifted towards longer wavelengths, see Figure 5.1(a) and (c). It can also be seen that the maximum extinction value of the peak increased up to a temperature above 100°C, where it reaches a top value. When the temperature is further increasing the signal starts to decrease, in combination with a distinct peak position shift to longer wavelengths. As I will show below in the MLWA theory section, this can be understood as an oxide shell forming around the metallic core until the particle is completely oxidized. The fact that Cu_2O oxide is formed is also corroborated by the specific absorption band appearing above 150°C, which corresponds to excitations of electrons above the band gap of Cu_2O oxide, which is 2.1 eV. Another interesting property is the small, but still observable, change of the extinction spectrum position right before the increase of the absorption band after 150°C. This indicate that another process occur here, it could be that the other copper oxide, CuO, is formed here.

For the reduction process, which was carried out in direct sequence to the oxidation after cooling the sample in oxygen atmosphere down to 50°C, the spectrum is initially not changing significantly and exhibits the characteristic absorption band for Cu_2O

oxide up to 200°C. There, quite suddenly, a new extinction band starts to appear at long wavelengths and shift rapidly to shorter wavelengths for further increase of the temperature, see Figure 5.1(b). This new extinction band then stabilizes with a maximum around 600 nm for temperatures above 250°C. This can be understood as the reverse process of what has been observed during oxidation, i.e., that a metallic nucleus, supporting plasmon resonance which give rise to the new extinction band that appears when the reduction starts, is formed either in the core (surrounded by an oxide shell) or as a shell around the oxide. The metallic part of the nanoparticle then steadily grows as oxide reduction proceeds faster with increasing temperature. The spectral blue shift observed is due to a decreasing amount of high refractive index oxide in the sensing volume of the plasmonic metallic part of the structure.

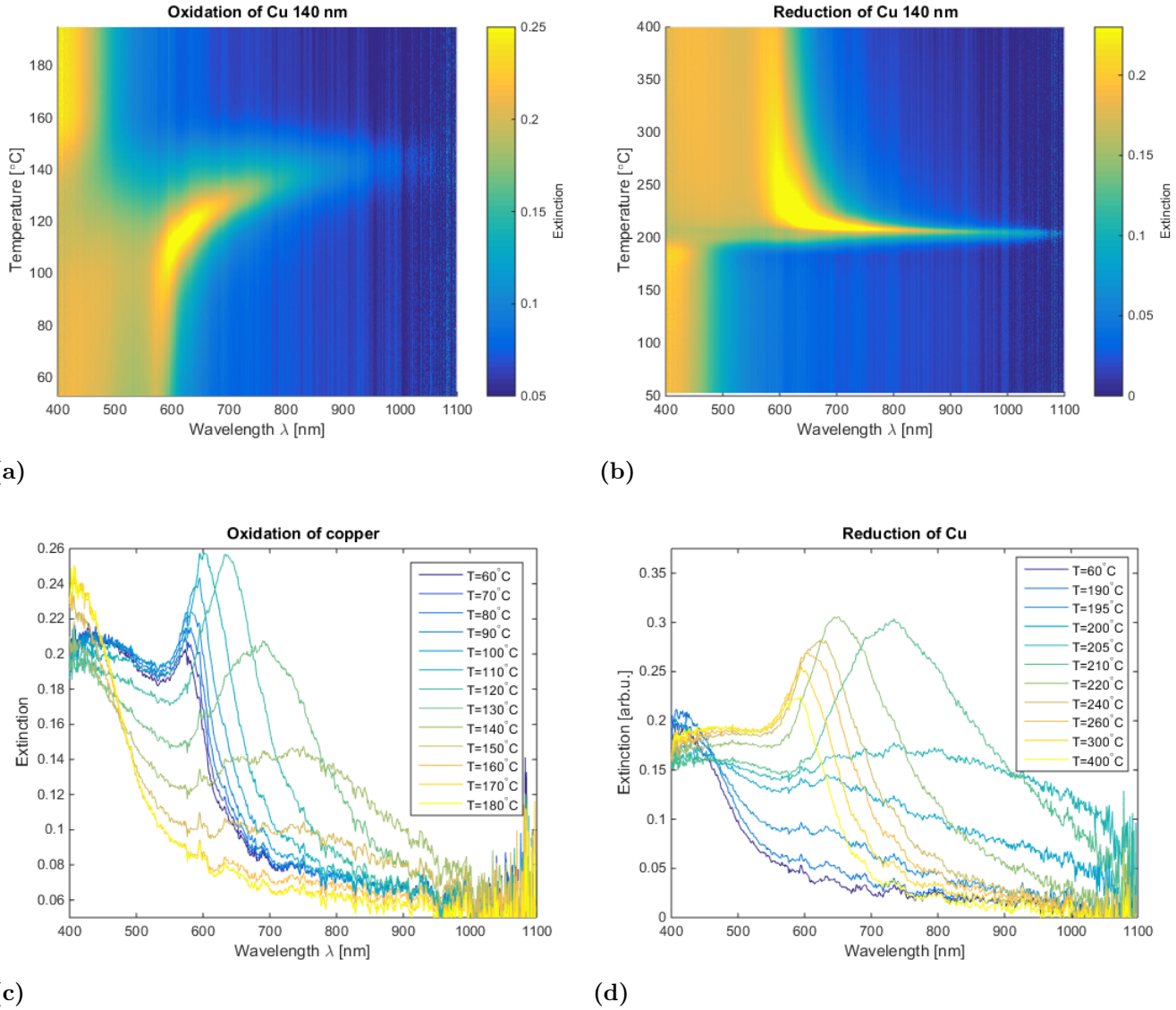

Figure 5.1: Optical spectra of 140 nm copper particles during heating in (a) and (c): oxidation phase, and (b) and (d): reduction phase.

To disambiguate the chemical composition of the samples when the Cu nanoparticles

were exposed to oxygen respectively hydrogen two complementary XPS experiments were done. The first one, shown in Figure 5.2 (a) was done on a sample that had been exposed to oxygen (2 vol% in Ar) in the reactor, with a temperature ramp up to 200°C and down to room temperature. The circumstances of the samples were therefore exactly the same as the ones during the optical measurements in the flow reactor. The satellite peaks in the XPS spectrum confirm that the sample contained CuO. The second experiment was done on the same sample, but after exposure to hydrogen (4 vol% in Ar) in a temperature ramp up to 400°C and down to room temperature. In Figure 5.2 (b) the satellite peaks are gone, which indicates that the sample was pure copper metal [35]. This proves that the reactor experiments with the given gas concentration of oxygen and hydrogen actually are oxidation respectively reduction processes, as anticipated from the *in situ* optical data.

The XPS spectrum of the second type of copper oxide, Cu_2O, is very hard to distinguish from the metallic Cu, due to a very close position of $2p_{3/2}$ peak [35]. It was however recognised that the $2p_{1/2}$ and $2p_{3/2}$ peaks are broader in Figure 5.2 (a) than in Figure 5.2 (b). This indicate that the formed oxides were both CuO and Cu_2O during exposure of 2 % O_2 up to 200°C. An additional study with an Auger Electron Spectroscopy (AES) measurement could further differentiate between Cu(I) oxide and Cu(II) oxide and verify the oxide formation.

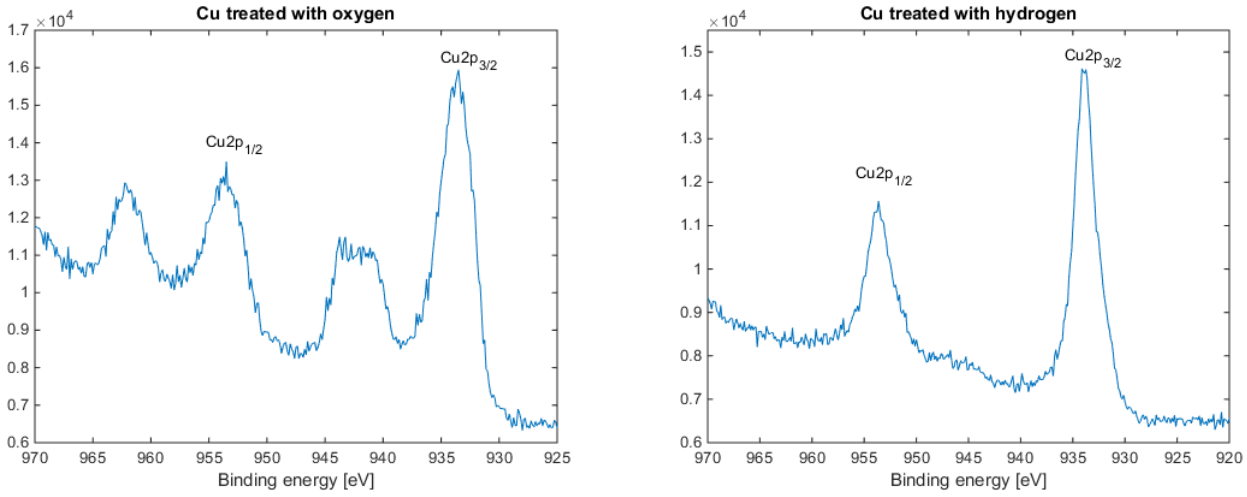

(a) **(b)**

Figure 5.2: XPS spectra of a 140 nm Cu sample where (a) was exposed to 2 % O_2 up to 200°C and (b) was exposed to 4 % H_2 up to 400°C.

5.1.1.1 Reversibility of oxidation and reduction processes

One long time experiment of nine cycles of reduction and oxidation was performed on copper, where the measured spectra were fitted with a 20th order polynomial function to extract the spectral position of the LSPR peak of the metallic copper core. The peak maximum extinction value during oxidation and reduction is pre-

sented in Figure 5.3 and the peak corresponding to the LSPR in the metallic Cu is presented in Figure 5.4. From both the measured parameters it is clear that the system acquire a stable correlation between the change of temperature/gas and the spectral position and value of the extinction peak, after a number of cycles of H_2/O_2 exposure. This indicates that the nanoparticles then have attained their equilibrium shape.

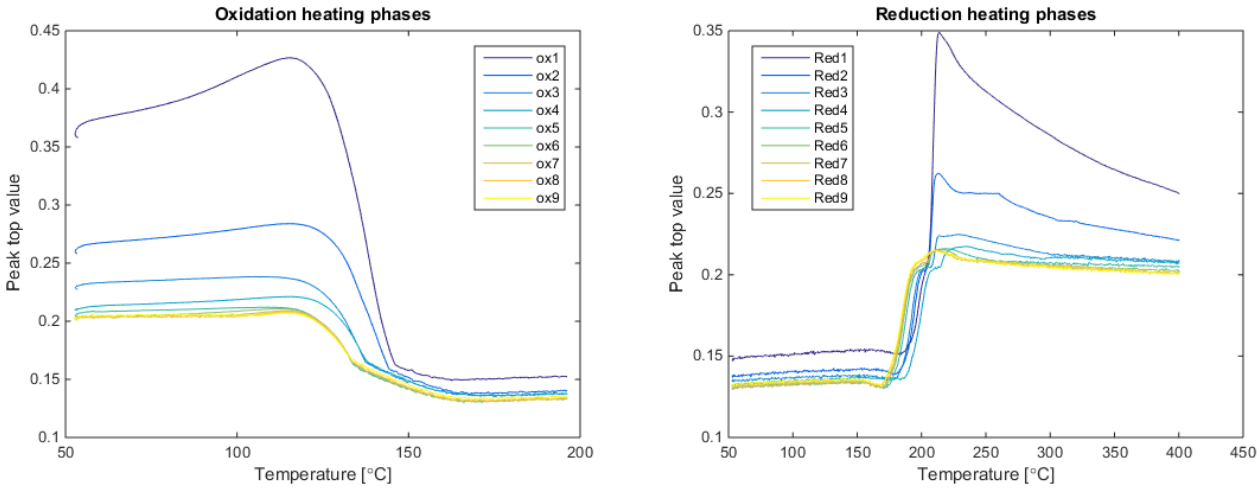

(a) **(b)**

Figure 5.3: Extinction at peak value of 140 nm Cu nanodisks during a heating ramp in (a) oxidizing and (b) reducing environment.

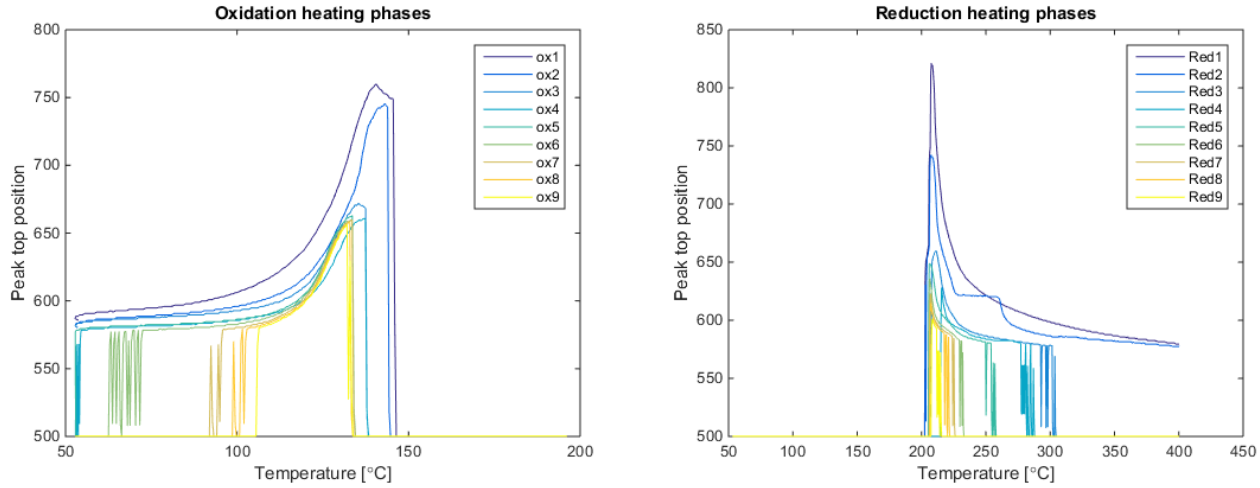

(a) **(b)**

Figure 5.4: Extinction peak position of 140 nm Cu nanodisks during a heating ramp in (a) oxidizing and (b) reducing environment.

To characterize the occurring structural changes, SEM images were taken, before

and after the experiment, both in the metallic state, see Figure 5.5. As can be seen, the projected particle diameter is relatively similar. However, the overall appearance of the particle is very different after oxidation-reduction cycling. The initial disk shape is replaced by a more layered structure of large crystalline domains.

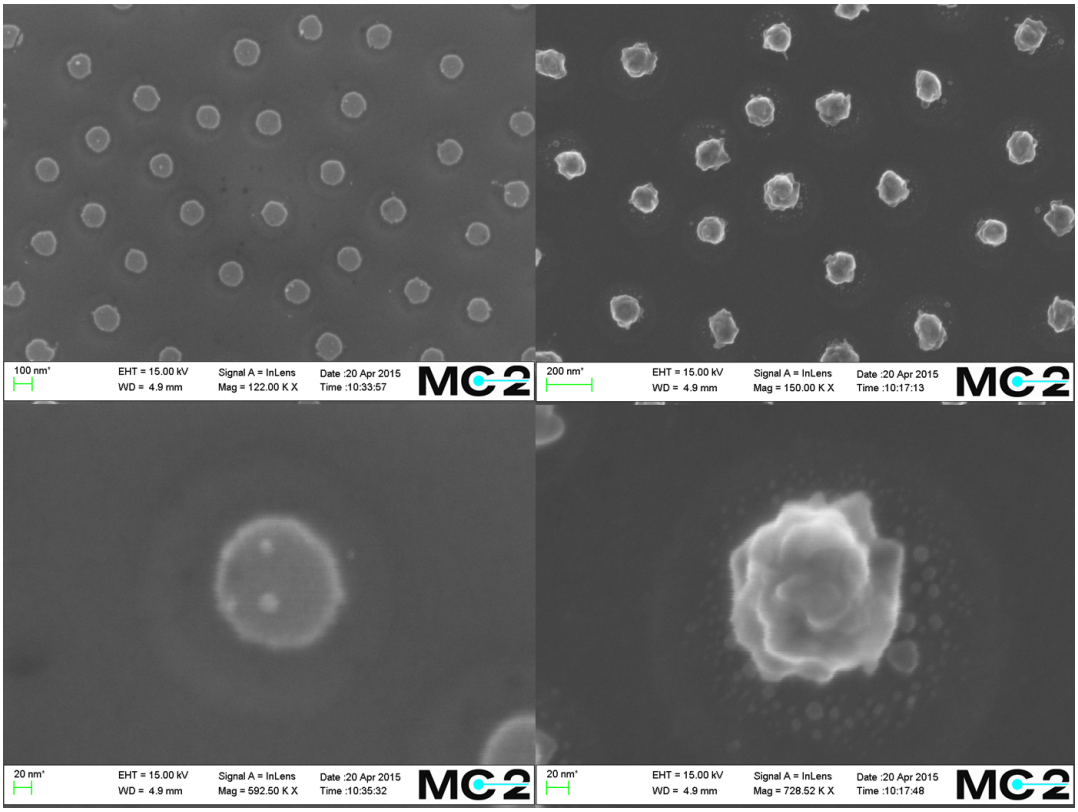

Figure 5.5: SEM images of copper particles, size 140 nm. The two left side pictures show the particles before treatment, i.e. directly after nanofabrication in the metallic state. The two pictures on the right side show the particles after treatment of nine cycles of oxidation and reduction, again also in the metallic state. Note that the magnifications are not the same in the corresponding images.

In order to relate how the temperature of the oxidation and reduction processes changed during the cycling experiments, and if there were any dependencies on Cu nanoparticle size, all experiments done on copper for different particle sizes (see appendix for the corresponding raw data) were analyzed. As readout parameters the end temperature of the oxidation and the start temperature of the reduction, both defined as the temperature where the peak position achieve its maximum value, were used. The corresponding data are shown in Figure 5.6. The results do not show any clear indication of size dependency in the considered particle size range. There is however a tendency of a decrease of the phase transition temperature during the first cycles, coinciding with the most severe restructuring of the nanoparticles. This indicates that there indeed is a dependence of these temperatures on the specifics of the microstructure of the nanoparticles. This could, for example, be related to different surface facets and their abundance.

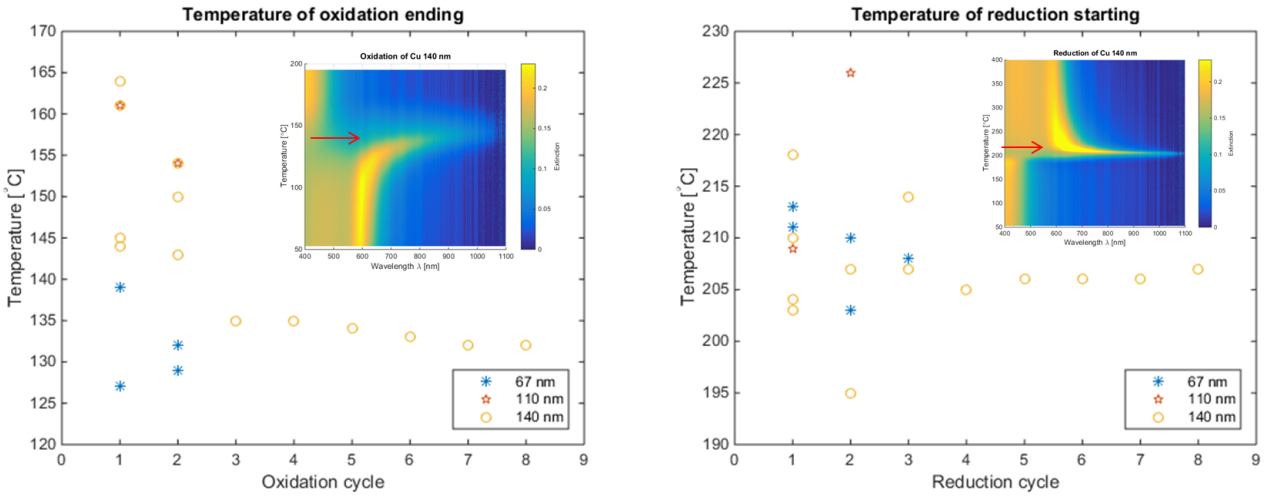

(a) **(b)**

Figure 5.6: A summary of all the temperature-controlled oxidation and reduction experiments on copper nanoparticles. (a) The temperature of the particles when they were fully oxidised, as a function of oxidation cycles for Cu particles of sizes 67, 110 and 140 nm. (b) The temperature when the particles started to reduce as a function of reduction cycles for Cu particles of sizes 67, 110 and 140 nm. The arrows in the insets indicate where in the spectra measurement the particles were assumed to be fully oxidised (a) respectively started to reduce (b).

5.1.2 Temperature programmed oxidation and reduction of cobalt nanoparticles

The results obtained from temperature-programmed oxidation and reduction experiments on cobalt nanoparticles were in various ways very different from the ones from copper. As a general trend, during the oxidation heating phase, see Figure 5.7 (a), the extinction band shifted to shorter wavelengths when the temperature increased, i.e. no red-shift of the LSPR peak, as observed for Cu, was observed for Co. It is also noticed that the peak position is more blue shifted already from the start and that the peak is broader for the Co nanoparticles, compared to the Cu ones. In the reduction heating step of the experiment, see Figure 5.7 (b), the spectrum of the sample was almost unchanged until a certain temperature where the extinction signal very abruptly almost vanishes. Interestingly, upon further temperature increase, also very abruptly, a new extinction spectrum appears, now absorbing over a much wider spectral range. This new broadening indicate that metallic cobalt was formed, which proves that the occurring circumstances, with 4 % H_2 exposure up to 500°C, reduces the particles completely.

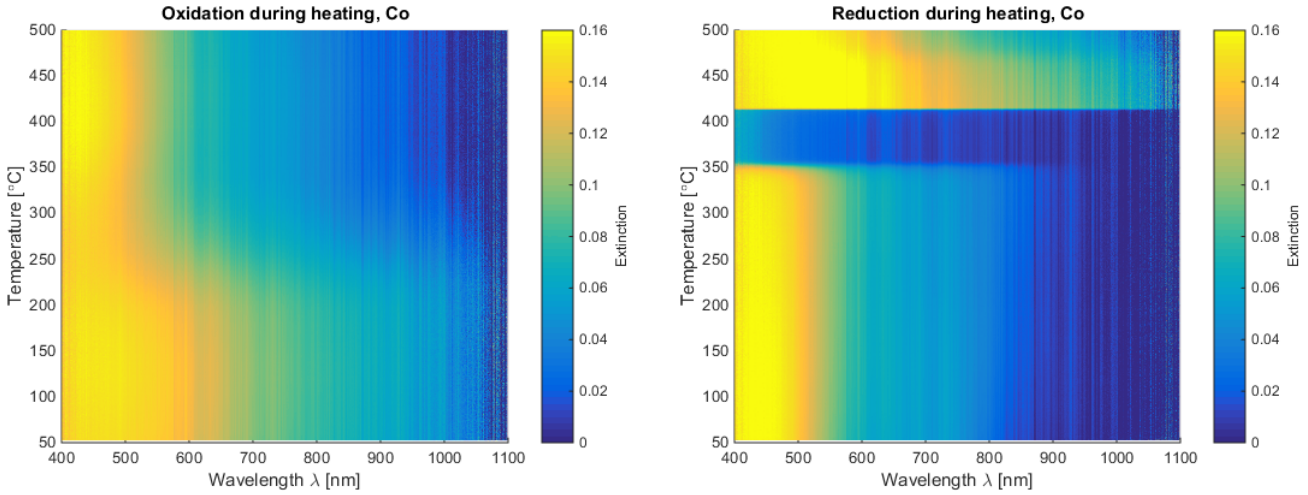

(a) **(b)**

Figure 5.7: Optical spectra of 140 nm Co particles measured during (a) an oxidation heating phase and (b) a reduction heating phase.

A more detailed picture of the transition from low extinction to high extinction in the temperature range between 410 and 418°C is shown in Figure 5.8. As can be seen, the transition occurs very rapidly and in a very narrow temperature range. Notably, the phenomenon occurred for all tested particle sizes repeatedly during reduction steps carried out in direct sequence with an oxidation.

The corresponding data for temperature ramps in inert argon is shown in the appendix. The decreased extinction spectra behaviour was not observed when exposing the samples to argon only. It was also noticed that the Co system did not behave the same if several temperature ramps hydrogen were carried out right after each

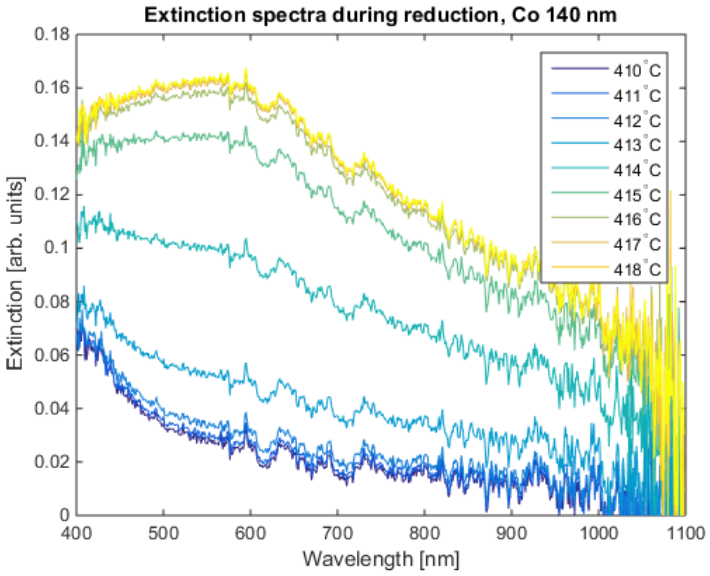

Figure 5.8: Measured extinction spectra for temperatures of 410-418°C in the vicinity of the upper observed phase transition for 140 nm Co nanoparticles. The figure shows that the transition is very fast in the specific temperature range.

other, see appendix Figure A.8. The transition periods were narrower and several steps seemed to occur for each cycle, which indicates that the observed sudden extinction drop is dependent on the oxidation state of the Co nanoparticles prior to the temperature in hydrogen, where the drop occurs.

The cooling phases of the temperature-controlled oxidation and reduction experiments are shown in Figure 5.9. In oxygen, i.e. when the Co is in an oxidized state, the spectral response is more or less unchanged. In hydrogen, i.e. when the Co is in the metallic state, we observe again a sharp and discrete broadband change in the optical response, at about 280°C . This, as seen during heating in hydrogen, probably indicates some kind of phase transition.

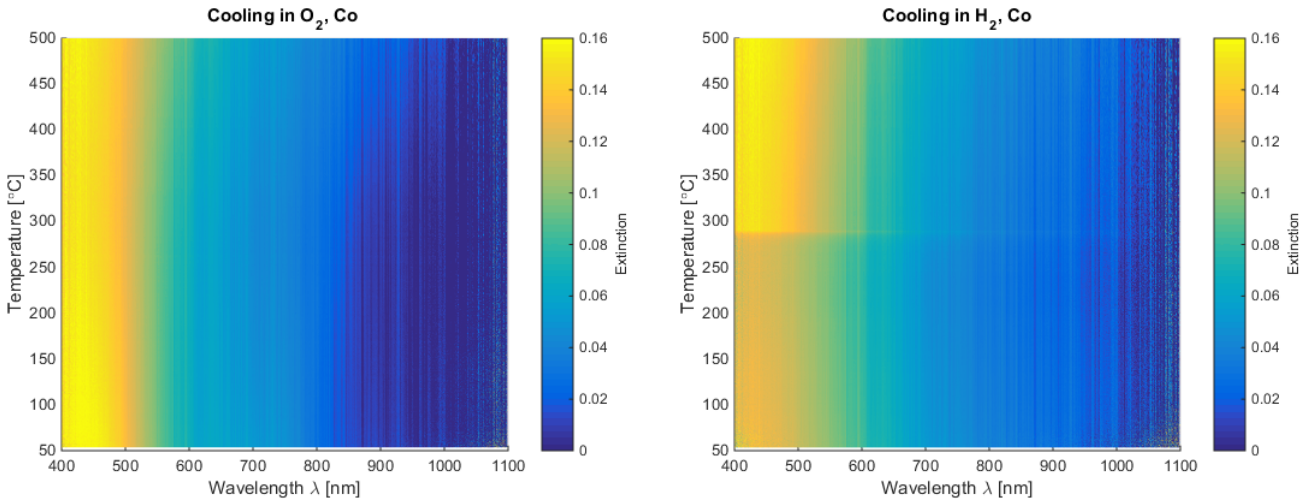

(a) **(b)**

Figure 5.9: Optical spectra of 140 nm Co particles measured during the cooling phase of a temperature-programmed oxidation (a), and temperature-programmed reduction (b) experiment.

Another interesting property of the Co nanoparticles was the optical response of the first exposure phases. In Figure 5.10 three different experiments are presented, where the newly fabricated and unreacted Co nanoparticles were exposed to Ar, see Figure 5.10 (a),(d),(g), H_2, see Figure 5.10 (b),(e),(h), and O_2, see Figure 5.10 (c),(f),(i). It was found that regardless which gas that was used during the first heating ramp after nanofabrication, a transition was observed. Notably, however, the temperature at which the transition occurred was quite different for the different gas environments.

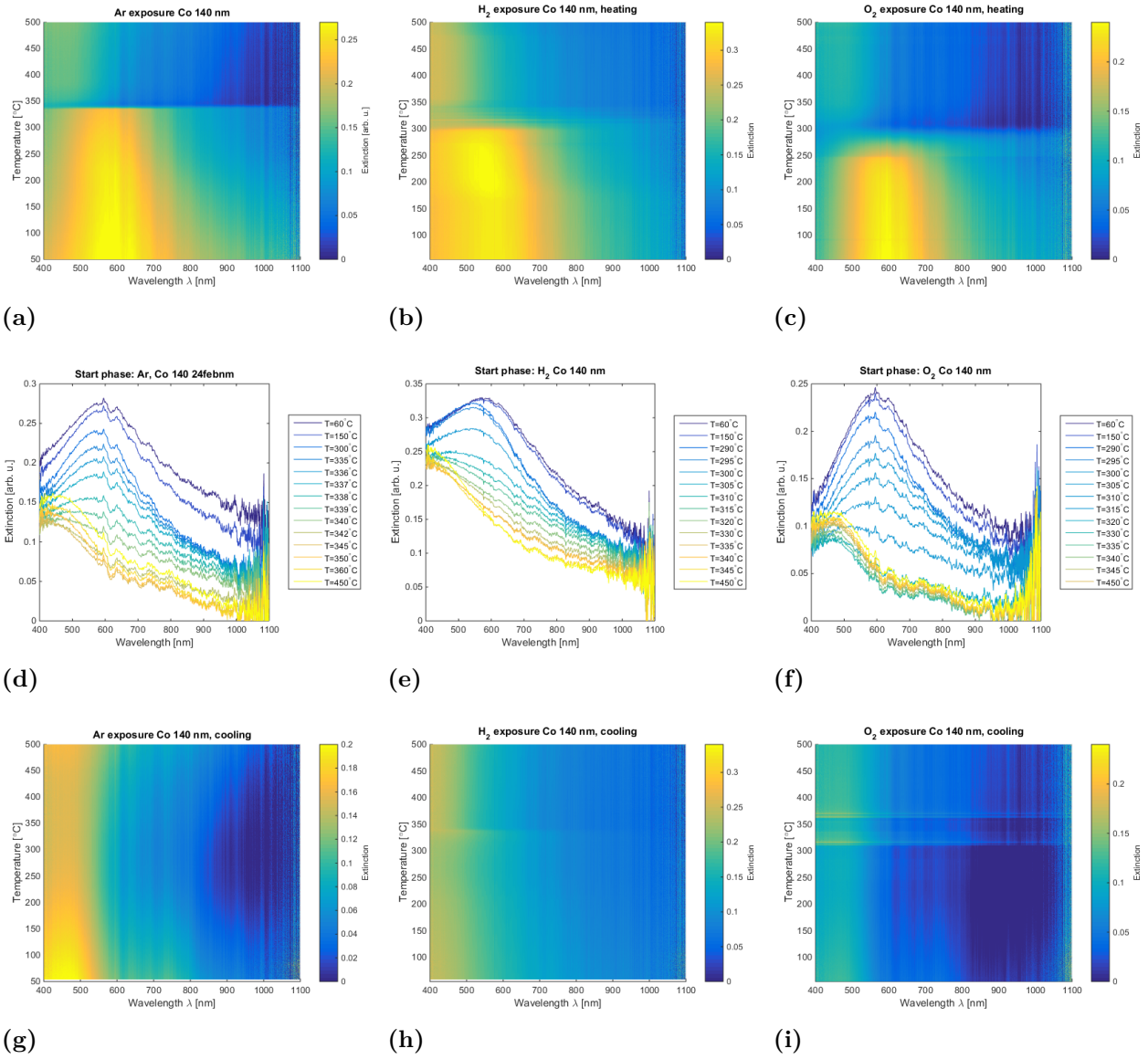

Figure 5.10: Optical spectra of 140 nm Co nanoparticles during heating and cooling in the first exposure cycle directly after nanofabrication. (a) and (d), (b) and (e), (g) and (h) show the spectra for Ar, H_2, respectively O_2 exposure during heating. (g), (h), and (i) show the spectra of Ar, H_2, respectively O_2 exposure during cooling.

As a first step to quantify the observed behaviour, an investigation of the start- and end temperature of the phase transition area (i.e. the temperature range with the characteristic extinction drop), was made, presented in Figure 5.11. The start temperature for the phase change occurred within the temperature range of 310-360°C for all investigated samples and after different amounts of cycling in hydrogen and oxygen. The small particles of size 67 nm (black line) have the lowest and most narrow transition range, and one of the tested 140 nm (blue dotted line) samples has the highest transition temperature, both for the start of transition, and for the end. The transition area of the 190 nm particles (red line) is located in between the areas of the 67 and 140 nm samples. There is therefore no clear size dependency, according to the experiments that were done. There is however a tendency of an equilibrium state of the transition temperature range after several cycles.

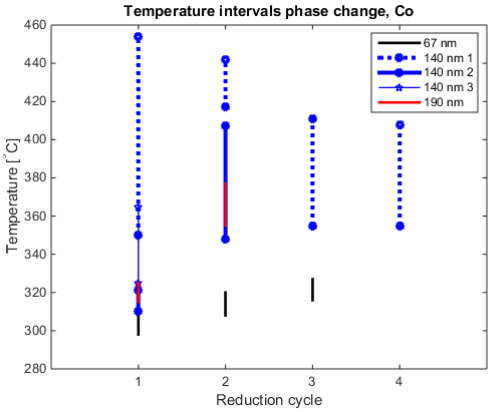

Figure 5.11: Temperature ranges wherein the cobalt samples stayed in the decreased extinction phase, as a function of the order of reduction cycle. Before each reduction the samples were exposed to oxygen up to 500°C.

To explain the observed behaviour of Co nanoparticles during reduction heating phase three different hypothesis can be suggested.

The first hypothesis is related to the so-called Kirkendall effect, which is an effect due to different diffusivities between a metal and its oxide. The theory is stating that the species in the metal core of the particle diffuses faster than the species in the outer oxide shell layer. This will create vacancies in the particle core, which leaves "Kirkendall voids". The phenomenon has previously been observed to occur in cobalt nanoparticles, from TEM studies of the oxidation and reduction states [36]. Specifically, in that study, for nanoparticles in the size range of 4-20 nm it was observed that the particles formed hollow Co_3O_4 particles after an oxidation process. When the particles were reduced, they broke up into smaller particles, of a size 60 % larger than the initial untreated ones.

In an attempt to identify the formation of Kirkendall voids in our system, SEM images of the investigated Co nanoparticles were taken before and after the heating and cooling of the particles in oxygen and hydrogen, shown in Figure 5.12. The corresponding optical spectra of the oxygen exposure during heating and the hy-

drogen exposure during heating are presented in Figure 5.13(a) respectively Figure 5.13(b). The initial diameter of the untreated particles, Figure 5.12 (a), was found to be 130 nm on average. After the oxidation at temperatures up to 500°C the particles increased their size to 145 nm on average. The following hydrogen exposure in a temperature ramp up to 500°C, did not result in any size change of the cobalt nanoparticles, but the surface structure seem to be more disordered. Moreover, the cobalt particles did not seem to form any voids or destruction of the inner shell that could be detected in SEM. Since the SEM image however, is not providing a cross section but only a top view, it is still not possible to rule out the formation of a void. At the same time we also do not know if the extinction drop effect is due to the reduction specifically, or only a restructuring effect of the additional heat treatment.

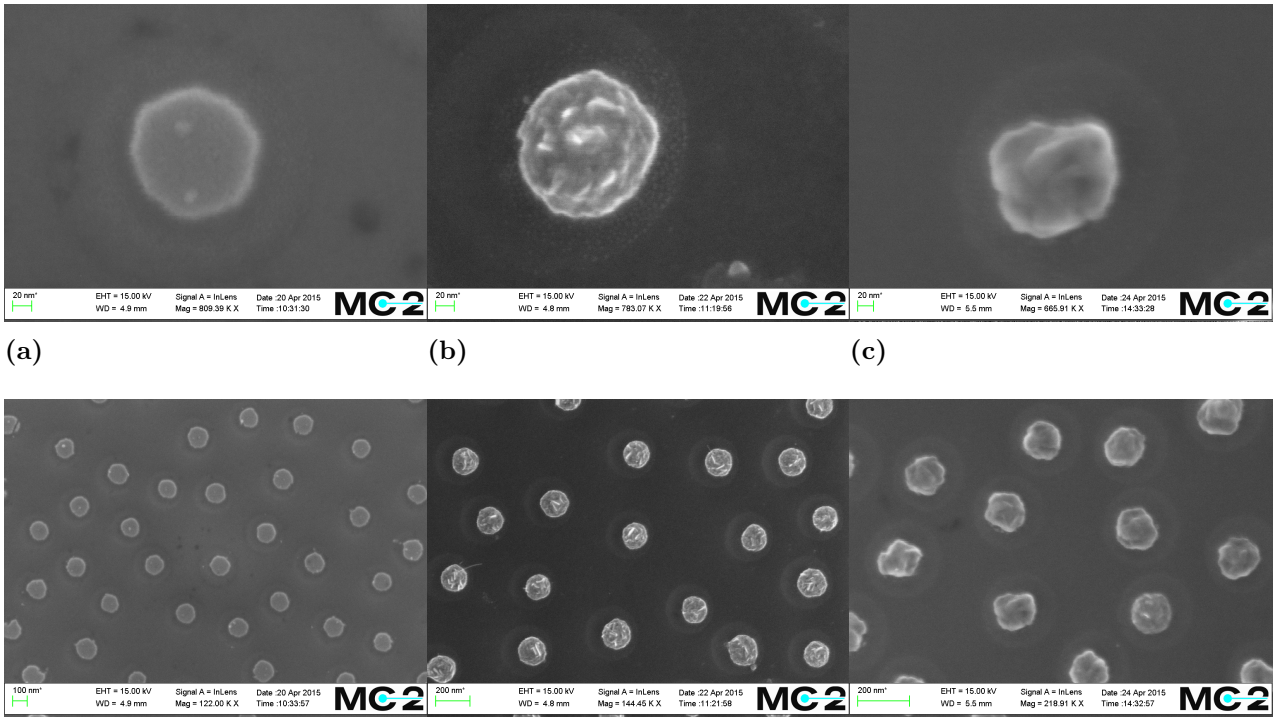

Figure 5.12: SEM images of Co particles when they were (a) and (d) untreated, (b) and (e) exposed to oxygen, (c) and (f) exposed to hydrogen. Note that the magnifications of the images are slightly different. The average projected diameter of the particles are (a) and (d) 130 nm, (b) and (e) 145 nm, (c) and (f) 145 nm

The second hypothesis is that the exposure to oxygen and hydrogen at the given temperatures was enough to oxidise respectively reduce the nanoparticles. The extinction spectrum drop could therefore be explained by subsequent formation of different oxides, whereof one has a bandgap large enough to not absorb light of the energies analyzed here. The formed bandgap could also be of indirect type, which would significantly decrease the absorption coefficient. The two oxides that probably are formed in the experiment are CoO and Co_3O_4. The first oxide, CoO, has a band gap reported to be 5 eV (248 nm) [37] and the latter one has two bandgaps at 1.5 eV (826 nm) and 2.0 eV (620 nm), respectively, due to that the most stable

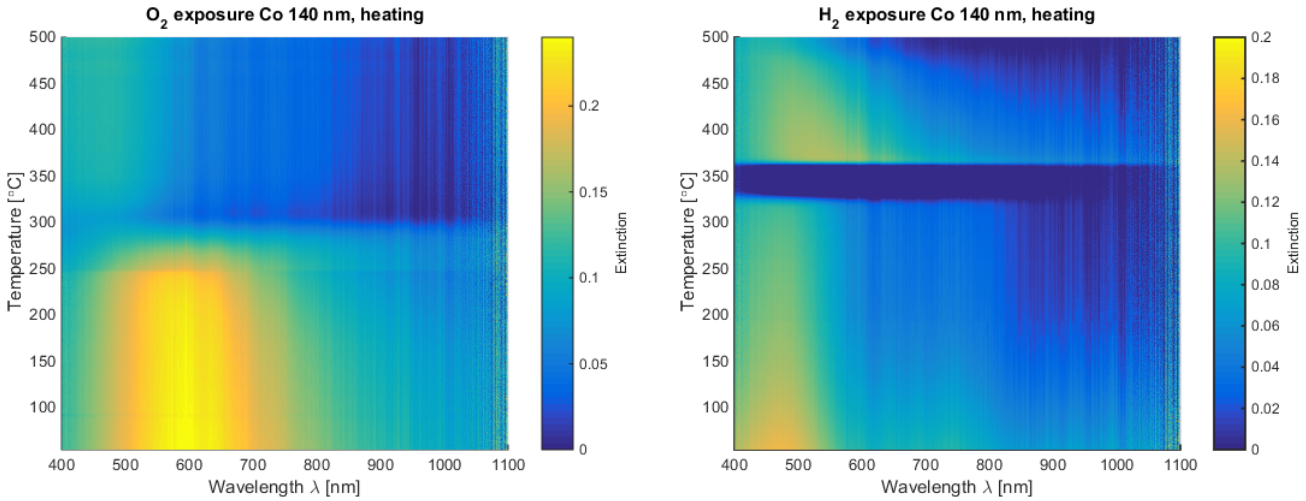

(a) (b)

Figure 5.13: Extinction spectra of the (a) oxidation process and (b) reduction process of cobalt nanoparticles of diameter 140 nm.

oxide form is Co(II)Co(III)$_2$O$_4$ [38]. The energies of the bandgaps of Co_3O_4 are in the area of the measurements. There is also one more kind of cobalt oxide, Co_2O_3, with a bandgap reported to be 4.0 eV [39], which corresponds to a wavelength of 310 nm which is outside of the measurement range. The intermittent formation of Co_2O_3 or CoO could therefore be an explanation of the rapid optical spectra change, supposed that the oxide formation is very fast.

The third hypothesis is that the observed abrupt change in the extinction spectra is due to crystallographic phase change between hexagonal close packed (hcp) structure and face centered cubic (fcc) structure, called a martensitic transformation. It has been found that martensitic transition of Co films takes place around 422°C and it has a weak first order character, which means, it induces a discrete jump in the enthalpy of formation value and sample volume at the transition temperature [40]. This is expected to be reflected in the optical/plasmonic properties. Moreover the oxidation and reduction behaviour of cobalt in the vicinity of the martensitic transformation has also been investigated before by Cabrera et al. [41]. They found that the prefactor of the exponential oxidation rate increased by several orders for temperatures higher than the transition temperature, between hcp and fcc. For other kind of magnetic alloys it has also been found that a martensite transformation will change the value of the permittivity[42]. Another study, by Stashchuk et al [43], claimed that the conductivity of cobalt is lower in the fcc crystal structure configuration, compared to the hcp structure. The conductivity is proportional to the imaginary part of the dielectric function, which is proportional to the absorption cross section, see Equation 2.18. Extinction is the sum of the absorption and scattering, and the latter one is small for the size of particles that we have tested. The extinction will therefore be decreased if the conductivity is decreased. The two possible effects of a martensitic transformation, where the lattice change between

hcp and fcc takes place, can therefore be summarized to:

1. Increased reaction rate of a certain cobalt oxide transformation, where the existence of CoO or Co_2O_3 occur in the phase change area.

2. Distinct change of the conductivity, as a direct consequence of the lattice configuration, which would have affected the extinction cross section.

The temperature-controlled oxidation and reduction experiments that we have done on cobalt nanoparticles did all show the extinction spectra decrease in the first exposure phase independent from which gas that was used, and for all reduction cycles that were in direct sequence with an oxidation cycle. We also saw that the transition occurred during cooling, but not as broad as in the heating of the nanoparticles. Another important point is that the transition did not behave the same for reduction phases that were in direct sequence with another reduction cycle. As discussed before, the transition area is almost not observable in these sequences. This indicates that it is required to oxidize the particles before we can observe any transition. This is however not in agreement with the results of the first-phase exposure experiment, see Figure 5.10, where the samples were assumed to be in metallic phase.

To generate further understanding of the possible origin of the made observations, a final experiment was done where a 30 nm thick Co film was deposited on a glass substrate. The purpose of this experiment is to elucidate if the observed optical feature around the martensitic transition and/or reduction of the oxide phase are specific to nanoparticles or not. Therefore, for the film, the reactor experiment was the same as before with varying cycle exposure of the film to hydrogen and oxygen at temperatures from 50°C to 500°C. In Figure 5.14 it is shown how the transmission spectrum through the film change during heating and cooling in hydrogen, directly after an oxidation step. The same kind of fast and distinct transition occurs also in this case, notably *both* in the heating and in the cooling phase. The main difference between the film and the particle experiments is the more apparent phase transition in the cooling phase, which probably corresponds to the reverse lattice structure transition as the heating phase in hydrogen. This indicates that the transition is reversible, which is an expected property of a martensite transformation. It is also noticed that the temperature of the cooling phase transition is higher than for the cooling phases for the nanoparticles, compare Figure 5.14 (b) and Figure 5.15. For the 67 nm Co particles, there was no transition observed in the cooling phase, see Figure 5.14 (a). There was however an observed double transition in the heating phase of the 67 mm Co particles, see Figure 5.16. This is an indication of a transition into a new phase in the first extinction drop, and then back again in the second extinction drop. For the larger particles, see Figure 5.15 (b) and (c), the transition temperature decreased with increase of particle size. Another interesting result from the experiment on Co film is that the absolute change of extinction is not as drastic as it is for the nanoparticles.

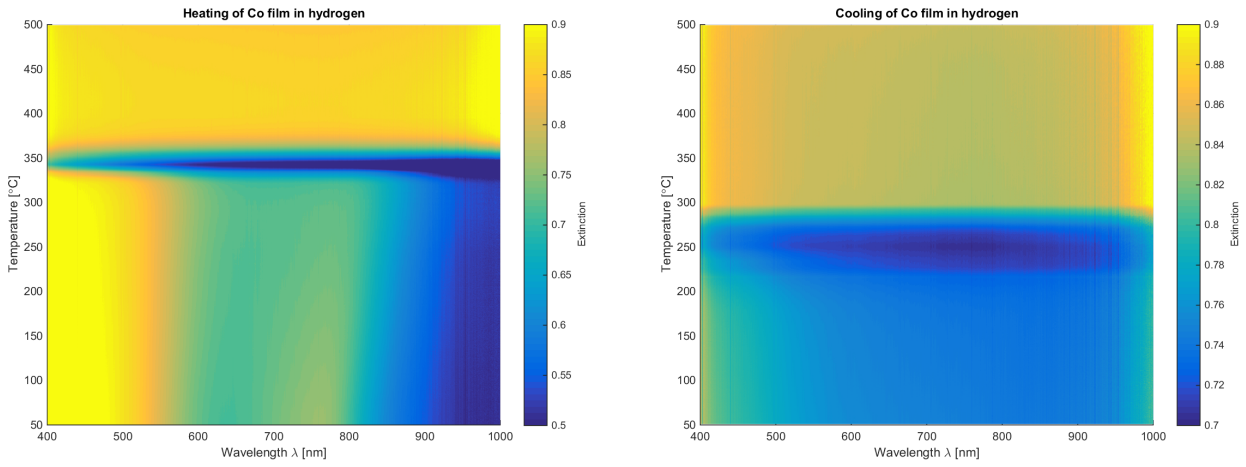

(a) **(b)**

Figure 5.14: Extinction spectra for a 30 nm thick Co film exposed to hydrogen during (a) heating and (b) cooling. The sample was exposed to oxygen at 500°C before this hydrogen cycle.

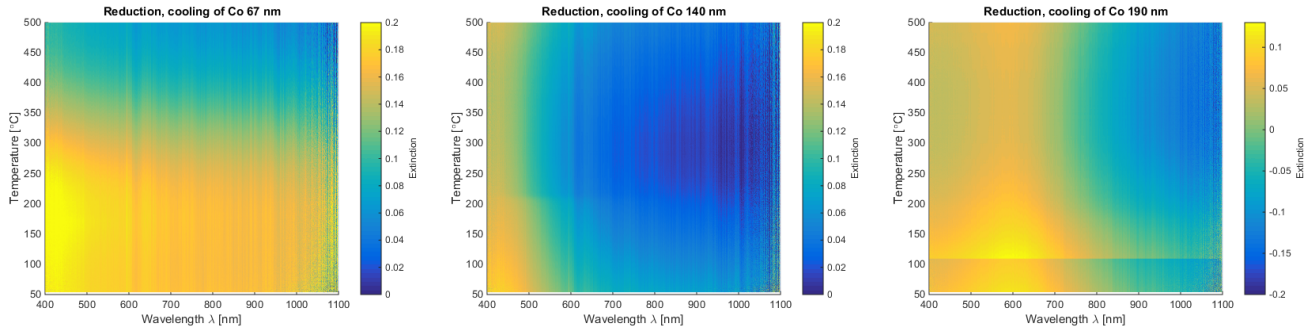

(a) **(b)** **(c)**

Figure 5.15: Extinction spectra of Co nanoparticles of the sizes (a) 67 nm, (b) 140 nm, (c) 190 nm during cooling in hydrogen.

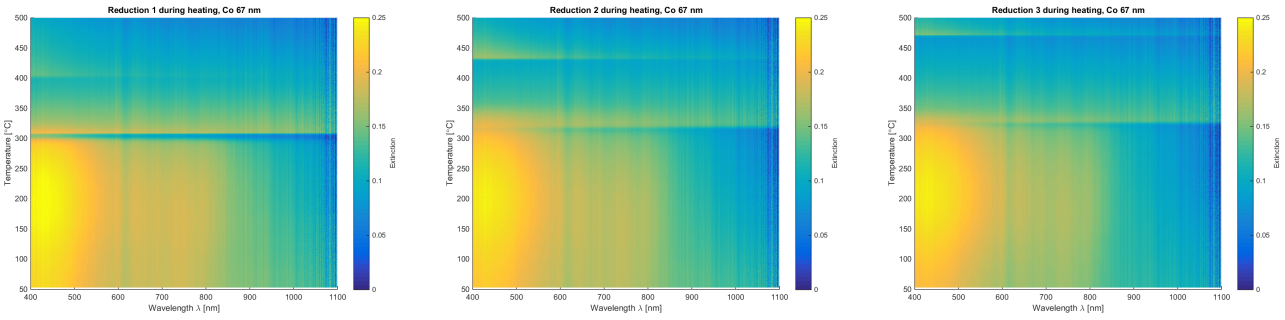

(a) **(b)** **(c)**

Figure 5.16: Extinction spectra of Co nanoparticles of size 67 nm during heating in hydrogen. Each hydrogen cycle is in direct sequence with an oxygen exposure cycle. (a) First reduction heating phase. (b) Second reduction heating phase. (c) Third reduction heating phase.

The first hydrogen exposure cycle of the Co film is shown in Figure 5.17. The extinction spectra are very similar during the heating process, until the transition range between 330-370°C. The cooling phase, see Figure 5.17 (b), signifies that the broad absorption spectrum characteristic for the film has been transformed into a more localized absorption regime in the UV range. This indicates that the film may have been transformed into particles during the treatment, with an LSPR in the UV for the metallic Co. This assumption is confirmed by an SEM analysis of the film before and after the experiment, see Figure 5.18. The SEM image of the film before the experiment does not show any kind of structure, but the image of the sample after experiment indicates that a particle-like structure has formed.

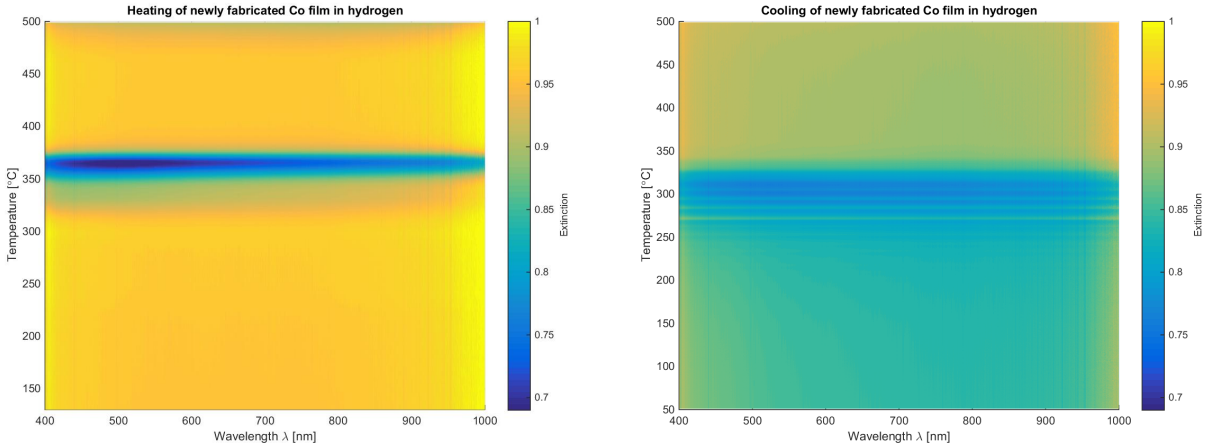

(a) **(b)**

Figure 5.17: First gas exposure cycle of the untreated Co film. (a) heating in H_2 and (b) cooling in H_2. Note that the colour scale is different in the two figures.

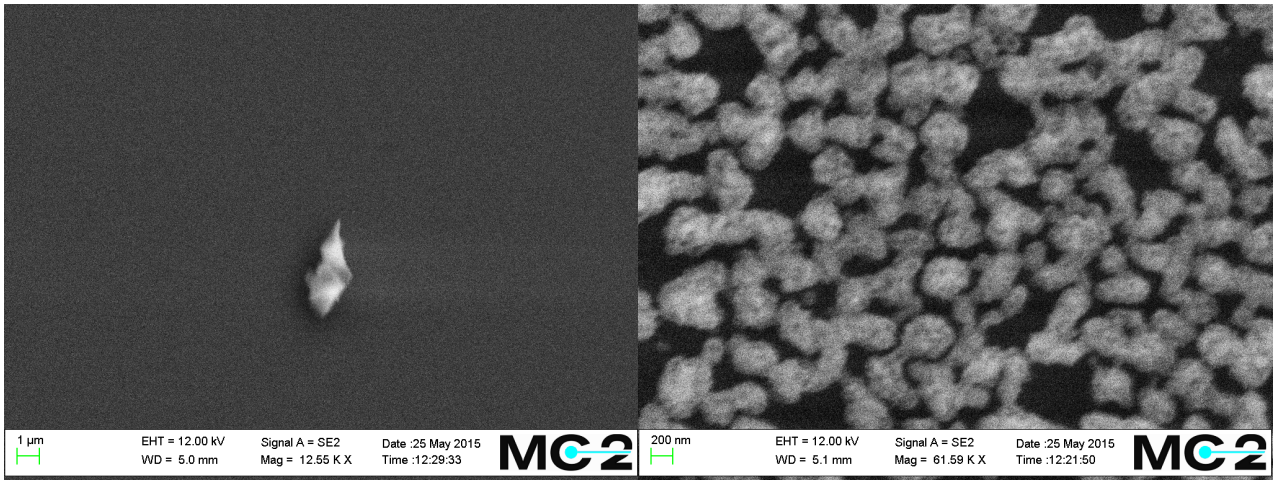

(a) **(b)**

Figure 5.18: SEM image of the Co film (a) before experiment, as deposited in the metallic state, (b) after the experiment. The structure seen in (a) is a dust particle on top of the sample, which is included to enable focusing of the electron beam in SEM and to show that the image actually is in focus.

Selected extinction spectra of the Co film in the temperature-programmed oxidation and reduction experiment are presented in Figure 5.19. The sample was in oxidised state before the hydrogen exposure, where after the oxygen exposure followed in direct sequence. The figure is therefore showing the same process as in Figure 5.14, but in this case for selected temperatures only, to highlight specific features. At 480°C of the Co film in O_2, see Figure 5.19 (b), the spectrum consists of two peaks, one at 814 nm and one at approximately 500 nm. These values corresponds quite well with the bandgap absorption edges of Co_3O_4 (826 eV and 620 eV).

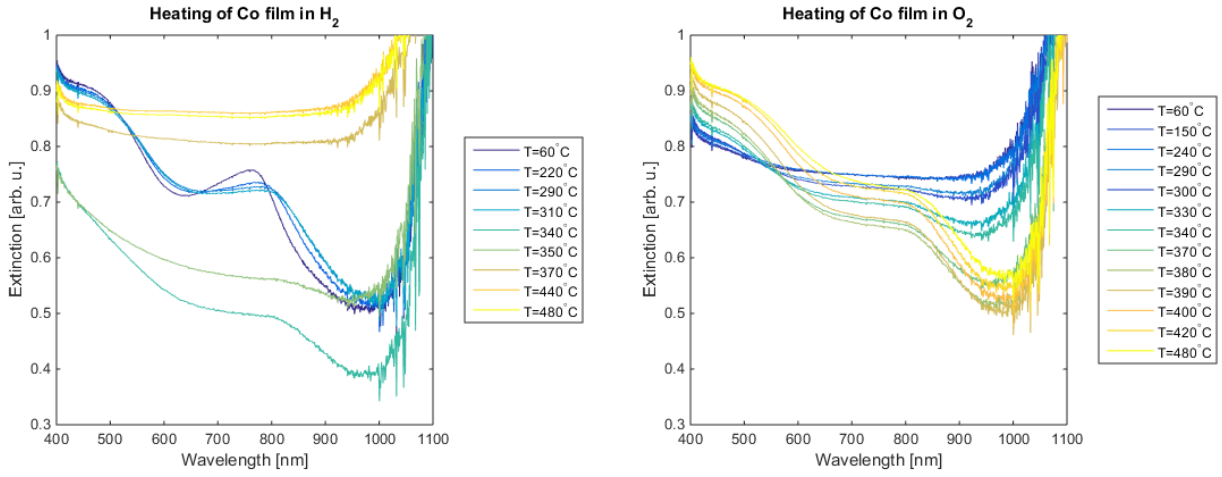

(a) **(b)**

Figure 5.19: Extinction spectra of Co film during heating in (a) H_2, (b) O_2 atmosphere. The sample was exposed to oxygen before the H_2 exposure in (a), where after the O_2 exposure in (b) followed in direct sequence.

A temperature ramp experiment in Ar is attached in Appendix A.4 where the optical spectra indicate that the exposing of Ar in temperature ramps up to 500°C will induce a drop in extinction only in the first temperature cycle. The subsequent cycles of temperature will yield the characterised band gap positions of Co_3O_4, as seen in the oxidation-reduction experiment on the other Co film, discussed above. This demonstrate an unwanted property of the "pure" Ar exposure experiment, that the gas and/or the reactor contains oxygen in such an extent that it will oxidise the Co film. The experiment also indicate another important point, that the transition regime does not occur for a temperature ramp where the sample is oxidised: the transition requires a transformation between oxide to reduced phase (metallic phase) to occur.

5.2 MLWA model computation

In order to relate the experimental results of the reactor experiments to a theoretical description, the MLWA model was used to compute the oxidation processes of copper and cobalt for an ideal oblate ellipsoid.

5.2.1 Copper

The dielectric functions for Cu and its oxides CuO and Cu_2O, which are used as input for the model, were adapted from Drobny et al. [44] and are shown in Figure 5.20 (a).

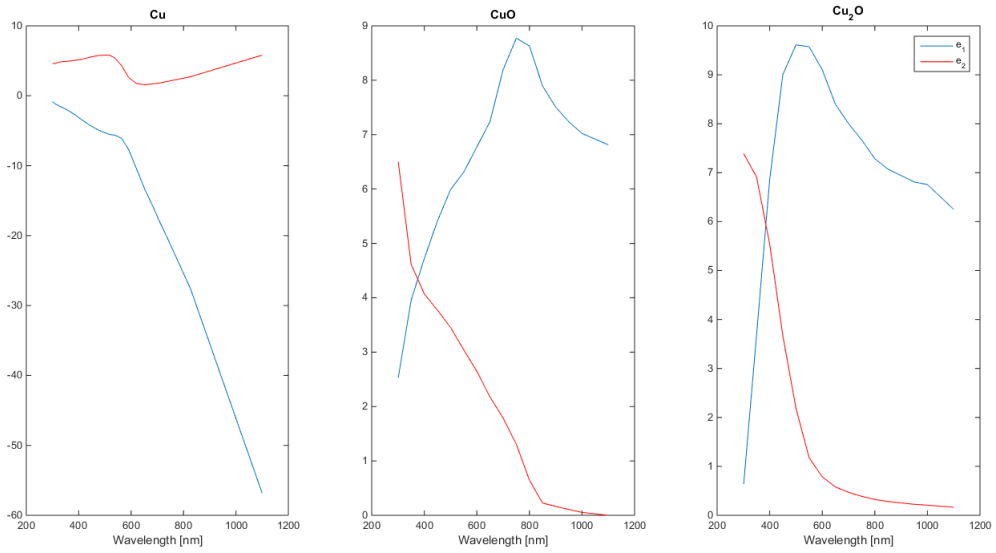

(a)

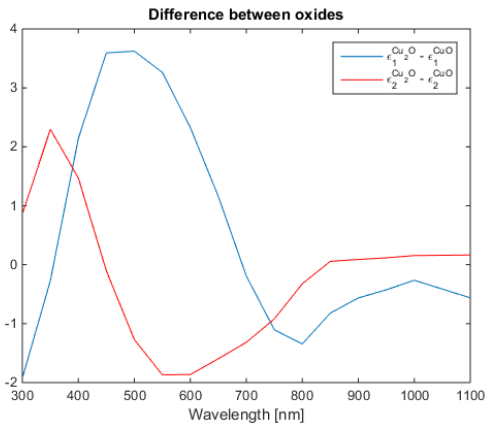

(b)

Figure 5.20: Dielectric functions of (a) Cu, CuO and Cu_2O [44] and (b) the difference of dielectric functions between Cu_2O and CuO. The red line corresponds to the real part (ε_1) and the blue to line the imaginary part (ε_2)

In Figure 5.21 (a),(b) MLWA calculations of the complete oxidation process are presented, assuming that a homogeneous shell of oxide is forming around a shrinking metallic core, and assuming a constant particle volume (i.e. not taking into account the volume increase in the oxide phase compared to the metal). The broad band optical response to the formation of a shell of the two different oxides is very similar. However, there are differences in the dielectric functions, see Figure 5.20 (b), where the real part is increased and the imaginary part is decreased for Cu_2O, compared to CuO.

The difference of the dielectric functions is affecting the extinction spectra, where the difference between the spectra (CuO formation - Cu_2O formation) is shown in Figure 5.21 (c). The blue area represents peak evolution of the oxide formation of Cu_2O and the yellow area the peak evolution of formation of CuO. It is noticed that the extinction peak of formation of CuO follows a slightly sharp peak position movement, and the formation of Cu_2O requires a bit higher ratio (0.82) of oxide formation in order to move the peak position to the end of measurement area, 1100 nm, compared to the required ratio of CuO (0.78).

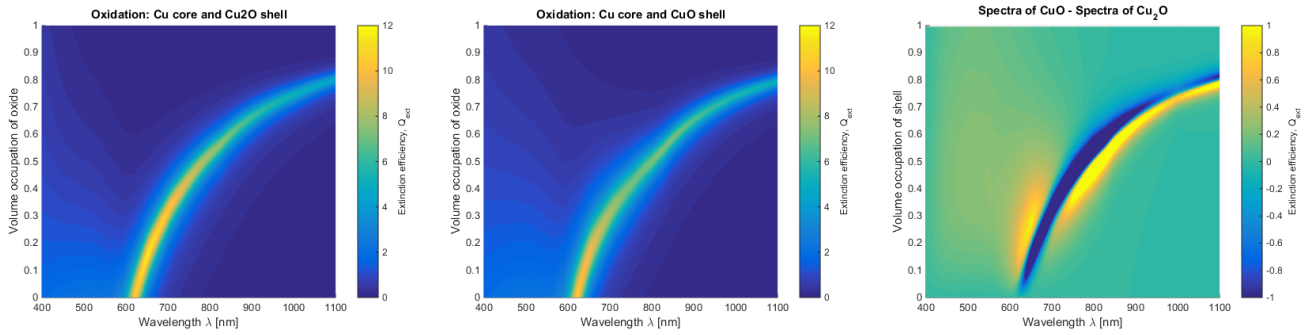

(a) **(b)** **(c)**

Figure 5.21: Simulation of oxidation process of a Cu core with increasing oxide thickness and its corresponding spectra. (a) Cu core and Cu_2O shell. (b) Cu core and CuO shell. (c) Difference between (b) and (a), where the yellow line shows the spectra evolution of the formation of CuO, and the blue area shows the evolution of formation of Cu_2O.

To further quantify the obtained data, we tracked the spectral position of the peak attributed to the LSPR in the copper core as well as the extinction at peak value as a function of oxide shell formation. The peak position and peak value are compared in Figure 5.22.

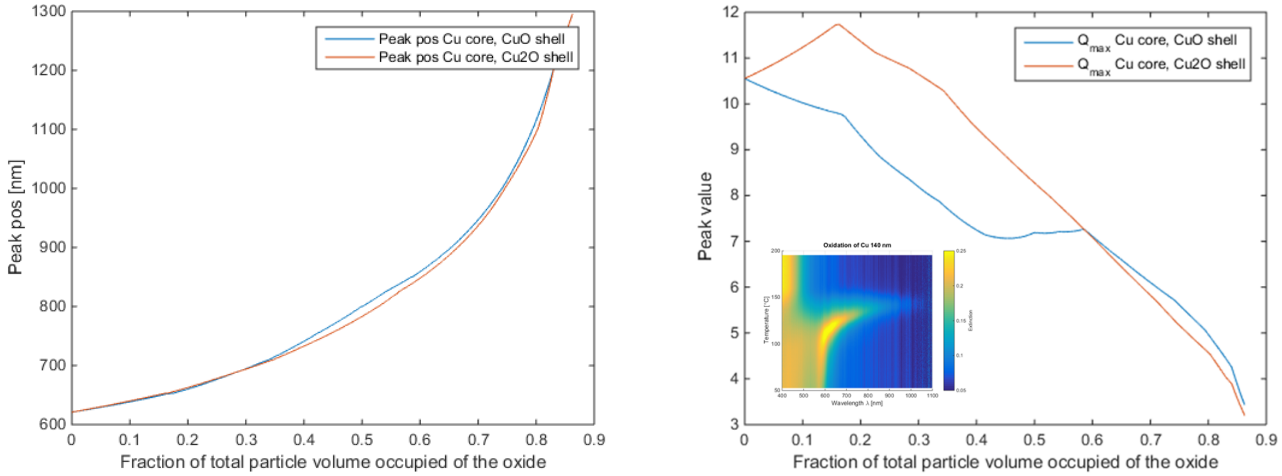

(a) **(b)**

Figure 5.22: MLWA simulation of (a) the peak position and (b) peak value, for oxidation process of a Cu core with increasing oxide thickness, where the inset in (b) is the experimental results of the optical spectrum evolution during the heating of Cu nanoparticles in oxygen.

The progress of peak position during the formation, see Figure 5.22 (a), of the two oxides are almost the same, with a slightly higher value for the CuO formation process (blue line). There is however a clear difference in the evolution of the peak extinction signal, see Figure 5.22 (b), which might help us investigate the oxide formation of our experiments. The initial increase of peak extinction value during formation of a Cu_2O shell looks very similar to the experimental results of copper oxidation spectra evolution, see the inset of Figure 5.22 (b). This may indicate that the formed oxide in the reactor experiments is predominantly Cu_2O.

Since it is well known that transition metals that allow different oxidation states may exhibit mixed oxides, it is interesting to apply MLWA simulation tool to investigate also a core shell modell, where the core/shell consists of CuO/Cu_2O or vice versa, i.e. Cu_2O/CuO. The corresponding simulation data are presented in Figure 5.23 where the optical response to the oxidation process of the different oxides as particle cores/shells is presented. The case with Cu_2O as core, Figure 5.23 (a), show a broadening behaviour and a slightly peak shift towards longer wavelengths during the oxide thickness growth. The other case, with CuO as core, Figure 5.23, presents the reverse scenario of a narrowing of the peak and a slightly peak shift towards shorter wavelengths as the shell increases. The comparison of the one-oxide particle scenario compared to the experiment is illustrated in Figure 5.23 (c). The spectrum of Cu_2O is rather constant until around 550 nm, where it rapidly increases. The spectrum of CuO increases its extinction value at a higher wavelength point, around 850 nm. The experiment seems to, beside from the planing of extinction value increase around 400 nm, correspond well with the spectrum of Cu_2O.

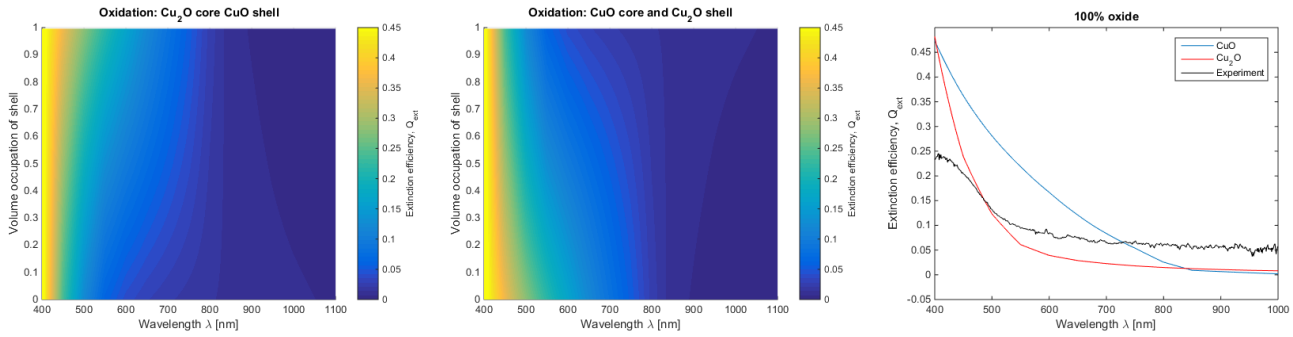

(a) **(b)** **(c)**

Figure 5.23: MLWA simulation of the oxidation process of (a) Cu_2O core with an increasing CuO shell and (b) CuO core with an increasing Cu_2O shell. (c) Spectra of particles consisting only CuO (blue line) and only Cu_2O (red line) and experimental data of spectrum from oxygen exposure experiment on copper particles at 200°C (black line).

The comparison of the MLWA simulation and the experiments of temperature-controlled oxidation of copper nanoparticles indicate that the formed oxide is Cu_2O. This assumption concurrent with the literature information, stated in section 3.3.1, that said that the formed oxide at 170°C is Cu_2O, and at 240°C it is CuO.

5.2.2 Cobalt

The data of dielectric function of Co and the oxides CoO and Co_3O_4 was rather hard to find for low energy. The used data of these was therefore restricted to the available wavelengths 300-560 nm, adapted from [45],[46] and [47], presented in Figure 5.24 together with the dielectric function for metallic Co. Based on the dielectric functions, the extinction efficiency spectra of an oblate spheroid with metallic Co core with an increasing oxide layer thickness was calculated, see Figure 5.25 (a),(b). The extinction spectra of the two cobalt oxides are quite similar, they move slightly towards longer wavelength and the value decreases, as the volume occupation of the oxide grows. There is however no tendency of a dramatic change of extinction, as the experimental ones did.

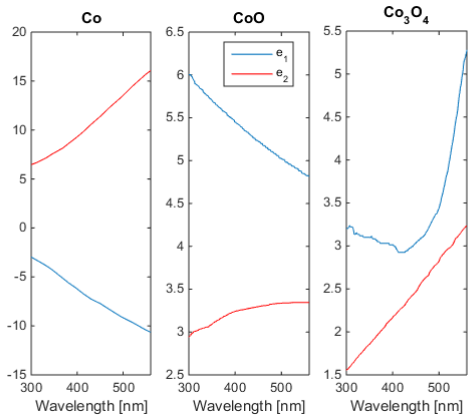

Figure 5.24: Dielectric function of Co [45], CoO [46] and Co_3O_4 [47] where the blue line corresponds to the real part (ε_1) and the red line to the imaginary part (ε_2). Due to lack of data the wavelength area is restricted to 300-560 nm.

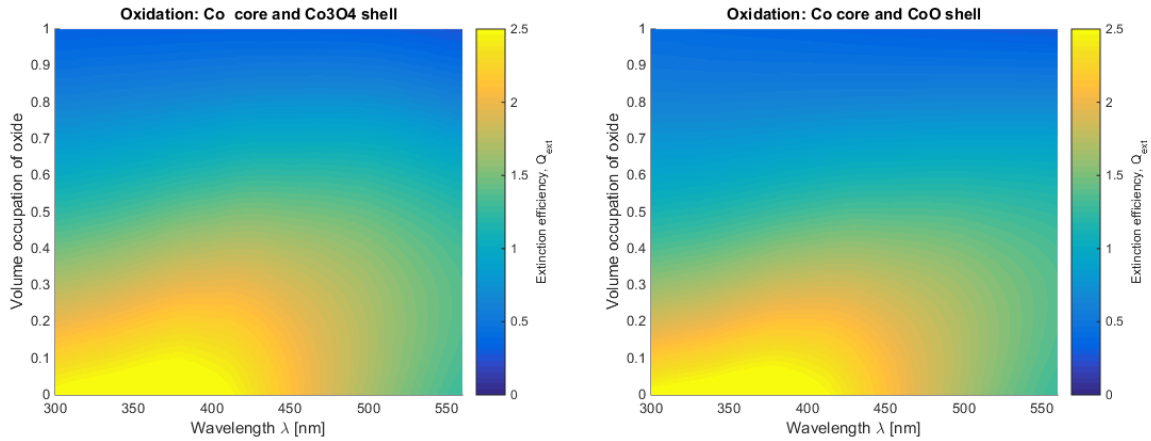

(a) **(b)**

Figure 5.25: MLWA simulation of oxidation process of a Co core with an increasing oxide shell thickness and their corresponding spectra.

The simulation of a CoO core particle with a shell oxide formation of Co_3O_4 is shown in Figure 5.26 (a). The extinction spectrum peak position moves from small wavelengths towards longer wavelengths and the signal value decreases, as the shell occupation of Co_3O_4 increases. Figure 5.26 (b) presents the reverse process: oxide formation of CoO as shell and Co_3O_4 as core. The situation is here the other way around, where the peak value decreases, and the peak position moves towards longer wavelengths, as the shell occupation increases. A comparison between the MLWA calculation and the temperature-programmed oxidation experiment of Co is shown in Figure 5.26 (c), where the blue line corresponds to an entirely oxidised CoO particle, the red line corresponds to an entirely oxidised Co_3O_4 particle, and black line represents the spectrum data, for the restricted wavelength area 400-560 nm, from an experiment of Co particles exposed with O_2 at 500°C. Due to the lack of data of the dielectric function for Co, it is hard to make any good comparison between the MLWA simulation and the experiment, but the experimental spectrum seems to stabilise into a maximum value near the experimental range end, at 400 nm. The spectrum of Co_3O_4 is also sustaining a maximum at this area, which make us conclude that the formed oxide of the experiment is Co_3O_4.

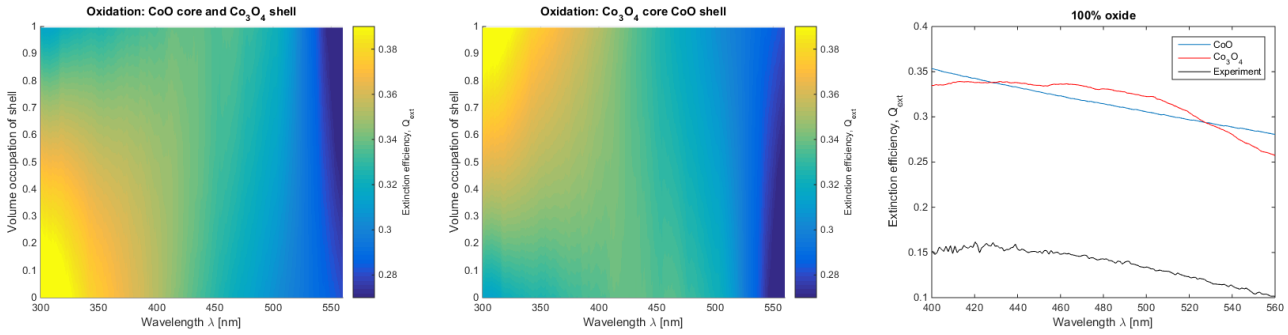

(a) **(b)** **(c)**

Figure 5.26: MLWA simulation of oxidation process of (a) CoO core with Co_3O_4 shell, (b) Co_3O_4 core with CoO shell, (c) spectra of particles consisting only CoO (blue line) and only Co_3O_4 (red line) and experimental data of spectrum from oxygen exposure experiment on copper particles at 500°C (black line).

The MLWA model could not explain the strange behaviour of the extinction spectra discrete jumping, of cobalt. The conclusion is therefore that it is not a matter of transition between the oxides and particles in itself that induce this effect.

5.3 Indirect plasmonic sensing

The first part of the INPS section was to find which fabrication parameters that afforded detectable samples in the reactor. The funneling approach has not been fully understood and controlled. The first samples were therefore not very successful, see Figure 5.27, where Cr rings around the structure are well shown.

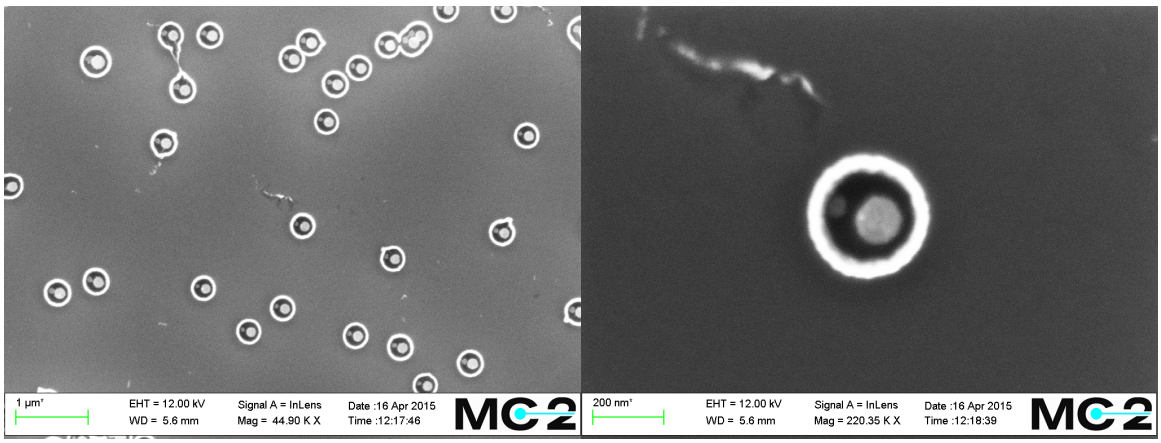

(a) **(b)**

Figure 5.27: Scanning electron microscope image of indirect sensing samples of 140 nm Au and 60 nm Cu with (a) 44.9k times magnification and (b) 220.36k times magnification. The bigger particle is Au, the smaller one is Cu. The white ring surrounding the structure is Cr.

The small size of the copper particles and low concentration of INPS structures made the signal low, which decreased the signal to noise ratio. To obtain a better signal the data was fitted with a Lorentzian function, where after it was filtered with a Savitzky-Golay function filter. The results, presented in Figure 5.28 and Figure 5.29 indicate that it might be possible to detect the copper oxidation process with the indirect sensing, but the signal response must be increased. The most clear result is shown in the reduction during heating plots of the peak value difference, Figure 5.28 (b), and the difference in peak position, Figure 5.29. At specific temperature points, around 150°C, the peak value difference decreases significantly, which indicate the reduction process.

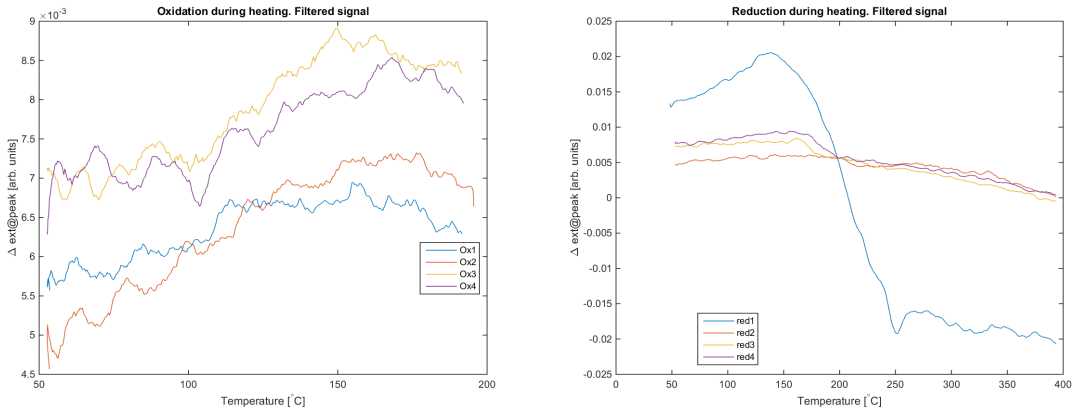

(a) **(b)**

Figure 5.28: Difference in peak value between the polarized light directions. (a) Oxidation. (b) Reduction.

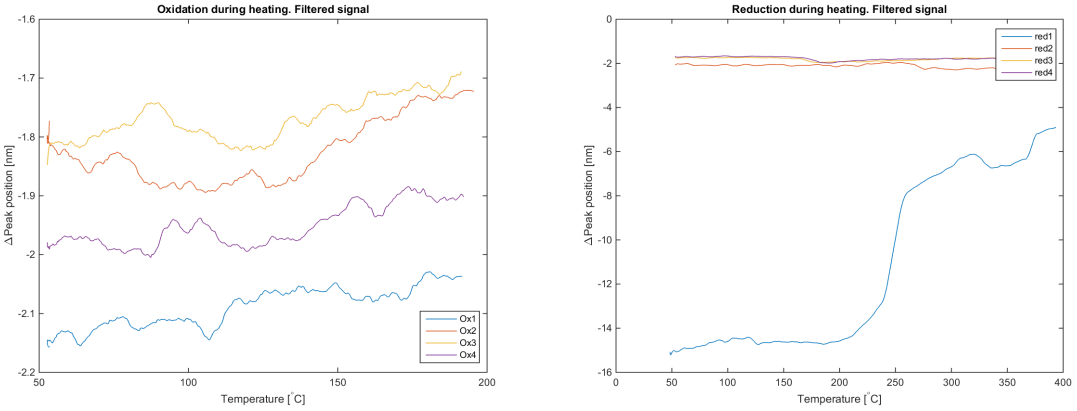

(a) **(b)**

Figure 5.29: Difference in peak position between the polarized light directions. (a) Oxidation. (b) Reduction.

6

Conclusions and outlook

The considered metal systems in this study, cobalt and copper, and their response of temperature and exposure of oxygen and hydrogen were in the previous chapter experimentally and computationally studied *in situ*. In this chapter the conclusions of the results will be presented. Moreover, I will indicate, which further research that has to be done to improve the knowledge of the correlation between oxidation states of metal nanoparticles and optical/plasmonic resonance response.

6.1 Oxidation and reduction properties of cobalt and copper

The results of the reactor experiments, SEM characterisation, XPS study, and MLWA model computation have all contributed to new insights of the redox properties of nanoparticles of the transition metals copper and cobalt.

6.1.1 Copper

The temperature-programmed oxidation and reduction experiments of copper nanoparticles yielded the most expected results, when comparing our data with the literature. The detection of the plasmonic resonance shift of particle discs of the diameters 67, 110 and 140 nm and height of 30 nm during oxidation and reduction was for all the experiments achievable. It was found that the oxidation process shifted the extinction peak position toward longer wavelengths, in agreement with a mechanism where oxide shell forms around a metallic core. The formed oxide was determined, by comparing the experimental results with the MLWA computation, to be predominantly Cu_2O for the used experimental environment of 2 vol% O_2 and temperature ramps up to 200°C. This is also in agreement with the XPS results, which yielded a mixture of Cu_2O and CuO. The reduction process of copper nanoparticles was found to have the similar, but reverse and faster, optical response as the oxidation, and the required temperature for the reduction was higher than for oxidation, above 200°C. Subsequent temperature-programmed oxidation and reduction cycles, together with the study of the corresponding structure evolution of the nanoparticles in SEM, showed that the copper nanoparticles can be reversibly oxidized and reduced over long time periods without loosing their plasmonic resonance properties in the metallic state. The particles required a couple of oxidation and reduction cycles before the signal response was constant, due to the necessary structural equilibration. There

was no clear particle size dependency of the observed oxidation and reduction temperatures, however, the onset of the respective process was observed to decrease for each oxidation and reduction cycle.

6.1.2 Cobalt

The cobalt nanoparticles were found to behave differently than the copper nanoparticle system. The exposure of oxygen to cobalt shifted the optical spectra towards shorter wavelengths and during the subsequent reduction a period in hydrogen, a temperature range of fast and distinct extinction decrease was observed. The phenomenon occurred for all reduction steps in direct sequence of an oxidation step. A similar optical signature could also be observed for all samples during the first temperature cycle directly after nanofabrication, independent from which gas the particles were exposed to. This result is, however, probably not due to the same mechanisms as for the sequent oxidation and reduction cycles. It is assumed that the optical response during the first temperature cycle is due to a pure restructuring phase of the newly nanofabricated samples. The same distinct optical change phenomenon was also found when exposing a Co film of thickness 30 nm to hydrogen in a linear temperature ramp up to 500°C. The treatment of the film during these circumstances was, however, found to transform the film into particle structures. The most probable explanation of the observed behaviour is concluded to be the martensitic transition, which is the crystallographic change of the lattice between hcp and fcc structure. The transformation between the lattices could have been inducing two different additional effects: either an increased reaction rate for the intermittent formation of CoO or Co_2O_3 that both have bandgaps outside of the measured spectral range (and thus would appear almost transparent), or an effect of a decreased value of conductivity in the metallic state, which is proportional to the extinction cross section. The MLWA simulation of cobalt oblate spheroids indicates that the formed oxide at the highest temperature was predominately Co_3O_4, in agreement with the literature.

6.1.3 Indirect sensing

It is expected that the optical cross section of smaller Co and Cu nanoparticles (<10 nm) in the direct sensing measurements would be very small. Thus, the indirect sensing scheme could make it possible to investigate much smaller structures without loosing accuracy. The few preliminary indirect sensing measurements done in this thesis give a good indication that the concept might work. However, the problem with residual Cr rings from the nanofabrication has to be solved first, before the indirect sensing strategy can be applied.

6.2 Outlook

The main goal of this thesis was to find correlations between different oxidation states of the transition metals cobalt and copper and their corresponding optical

and plasmonic resonance response. This project has been a small but also important step forward on that way. My hope, and also my expectation, is that the plasmonic sensing in the future can be a well used tool for investigation of material properties and reaction behaviours. I have chosen a few important areas where the usage of localized plasmonic nanoparticles, based on the findings in this project, needs to be further investigated in order to make it to a candidate for material sensing.

In a first sense the copper and cobalt system have to be studied more and for a wider range of particle sizes both in the direct and indirect sensing configuration. The chemical composition during different circumstances has to be analyzed more in detail, where Auger electron spectroscopy analysis of copper and cobalt would have been a good choice, due to the separated peaks of the oxides [35]. To enable the plasmonic sensing technique to be cost effective we also need to find how certain single wavelengths behave during oxidation and reduction, in order to decrease the cost for sensing by using cheaper diodes, which would be a crucial property if the concept should be adapted into the industry and other research areas.

Apart from the rather straightforward future prospects of plasmonic sensing the following exciting areas have to be analysed in order to increase the knowledge of catalytic reactions.

6.2.1 Mass spectrometry

It would have been possible to connect a mass spectrometer to the output of the mass-flow reactor, to enable a detection of how the consumption of oxygen and hydrogen changed over the process for different temperatures. This would give an indication of how the kinetics of the oxidation and reduction are changing over time and for different circumstances, such as temperature and size of catalyst nanoparticles. By relating the output of the mass spectrometry measurements with the optical signal response, plasmonic sensing could be a complement to other kinetic measurement tools, such as temperature programmed desorption (TPD) experiments.

6.2.2 Sintering

One of the most essential deactivation mechanisms of catalysts is sintering, the fusing of small particles into bigger ones. The process reduces the surface area, which will decrease the reaction rate. The plasmonic response does therefore need to be related to the sintering mechanism, by measuring the structure, such as particle height and diameter, in situ. By doing single particle studies it is possible to investigate how a specific particle change over time in the SEM.

6.2.3 Simulation

The MLWA model that was used in this project was a good tool in order to compare the oxidation and reduction behaviour of the experiments with different models of

oxide formation for the size of 140 nm. In catalysis the size of particles often is much smaller. For particles where the size is comparable to the mean free path of electrons, quantum effects must be considered, which embrace ab initio quantum mechanical computations. It is important to understand the underlying mechanisms of plasmonic sensing and the size effects, to increase the accuracy of the tool.

Bibliography

[1] F. Wei, Z. W. Chen, and W. M. Gibson. Measurement of oxidation states for transition elements with a small spot tabletop xanes instrument. *X-Ray Spectrometry*, 38(5):382–385, 2009.

[2] Rejiya C.S., Jatish Kumar, Raji V., Vibin M., and Annie Abraham. Laser immunotherapy with gold nanorods causes selective killing of tumour cells. *Pharmacological Research*, 65(2):261 – 269, 2012.

[3] David Conklin, Sanjini Nanayakkara, Tae-Hong Park, Marie F. Lagadec, Joshua T. Stecher, Xi Chen, Michael J. Therien, and Dawn A. Bonnell. Exploiting plasmon-induced hot electrons in molecular electronic devices. *ACS Nano*, 7(5):4479–4486, 2013. PMID: 23550717.

[4] Christoph Langhammer, Elin M. Larsson, Bengt Kasemo, and Igor Zorić. Indirect nanoplasmonic sensing: Ultrasensitive experimental platform for nanomaterials science and optical nanocalorimetry. *Nano Letters*, 10(9):3529–3538, 2010. PMID: 20718400.

[5] Craig F. Bohren and Donald R. Huffman. *Absorption and Scattering of Light by Small Particles*. Wiley-VCH Verlag GmbH, 2007.

[6] K. Lance Kelly, Eduardo Coronado, Lin Lin Zhao, and George C. Schatz. The optical properties of metal nanoparticles: The influence of size, shape, and dielectric environment. 107(3):668–677, 2003.

[7] Heinz Raether. *Surface Plasmons*. Springer-Verlag Berlin Hedelberg, 2007.

[8] Paul Mulvaney. Materials mix. optical properties of metal clusters by u. kreibig, m. vollmer, springer series in materials science, vol. 25, springer, berlin 1995, xvii, 532 pp., hardcover, dm 98.00, isbn 3-540-57836-6. *Advanced Materials*, 8(8):699–699, 1996.

[9] C. Langhammer. *Nanoparticles plasmons in classic and novel materials - Fundamentals and hydrogen sensing*. PhD thesis, Chalmers university of technology, 2009.

[10] A. S. Kirakosyan, M.I. Stockman, and T. V. Shahbazyan. Surface plasmon lifetime in metal nanoshells. 2009.

[11] A. Wokaun, J. P. Gordon, and P. F. Liao. Radiation damping in surface-enhanced raman scattering. *Phys. Rev. Lett.*, 48:957–960, Apr 1982.

[12] Christoph Langhammer, Bengt Kasemo, and Igor Zorić. Absorption and scattering of light by pt, pd, ag, and au nanodisks: Absolute cross sections and branching ratios. *The Journal of Chemical Physics*, 126(19), 2007.

[13] George H. Chan, Jing Zhao, Erin M. Hicks, George C. Schatz, and Richard P. Van Duyne. Plasmonic properties of copper nanoparticles fabricated by nanosphere lithography. *Nano Letters*, 7(7):1947–1952, 2007.

[14] Christoph Langhammer, Igor Zorić, Bengt Kasemo, and Bruce M. Clemens. Hydrogen storage in pd nanodisks characterized with a novel nanoplasmonic sensing scheme. *Nano Letters*, 7(10):3122–3127, 2007. PMID: 17850168.

[15] Krijn P. de Jong. *Synthesis of Solid Catalysts*. Wiley-VCH Verlag GmbH & Co. KGaA, 2009.

[16] I. Chorkendorff and J. W. Niemantsverdriet. *Concepts of Modern Catalysis and Kinetics*. Wiley-VCH Verlag GmbH, 2006.

[17] Thomasz J Antosiewicz, Carl Wadell, and Christoph Langhammer. Plasmon-assisted indirect light absorption engineering in small transition metal catalyst nanoparticles.

[18] X. Zhang, X. Ke, A. Du, and H. Zhu. Plasmonic nanostructures to enhance catalytic performance of zeolites under visible light. *Scientific Reports.*, 4, 2014.

[19] Andiappan Marimuthu, Jianwen Zhang, and Suljo Linic. Tuning selectivity in propylene epoxidation by plasmon mediated photo-switching of cu oxidation state. *Science*, 339(6127):1590–1593, 2013.

[20] P. Christopher, H. Xin, and S. Linic. Visible-light-enhanced catalytic oxidation reactions on plasmonic silver nanostructures. *Nature Chemistry*, 3:467–472, 2011.

[21] Sabine Schimpf, André Rittermeier, Xiaoning Zhang, Zi-An Li, Marina Spasova, Mauritz W.E. van den Berg, Michael Farle, Yuemin Wang, Roland A. Fischer, and Martin Muhler. Stearate-based cu colloids in methanol synthesis: Structural changes driven by strong metal–support interactions. *ChemCatChem*, 2(2):214–222, 2010.

[22] Joon B. Park, Jesus Graciani, Jaime Evans, Dario Stacchiola, Sanjaya D. Senanayake, Laura Barrio, Ping Liu, Javier Fdez. Sanz, Jan Hrbek, and José A. Rodriguez. Gold, copper, and platinum nanoparticles dispersed on ceox/-tio2(110) surfaces: High water-gas shift activity and the nature of the mixed-metal oxide at the nanometer level. *Journal of the American Chemical Society*, 132(1):356–363, 2010. PMID: 19994897.

[23] Andrew A. Peterson, Frank Abild-Pedersen, Felix Studt, Jan Rossmeisl, and Jens K. Norskov. How copper catalyzes the electroreduction of carbon dioxide into hydrocarbon fuels. *Energy Environ. Sci.*, 3:1311–1315, 2010.

[24] Pascal Lignier, Ronan Bellabarba, and Robert P. Tooze. Scalable strategies for the synthesis of well-defined copper metal and oxide nanocrystals. *Chem. Soc. Rev.*, 41:1708–1720, 2012.

[25] Sally D. Solomon, Susan A. Rutkowsky, Megan L. Mahon, and Erica M. Halpern. Synthesis of copper pigments, malachite and verdigris: Making tempera paint. *Journal of Chemical Education*, 88(12):1694–1697, 2011.

[26] Akihiro Yabuki and Shuji Tanaka. Oxidation behavior of copper nanoparticles at low temperature. *Materials Research Bulletin*, 46(12):2323 – 2327, 2011.

[27] G. W. Poling. Infrared reflection studies of the oxidation of copper and iron. *Journal of The Electrochemical Society*, 116(7):958–963, 1969.

[28] Hui Wang, Felicia Tam, Nathaniel K. Grady, and Naomi J. Halas. Cu nanoshells: Effects of interband transitions on the nanoparticle plasmon resonance. *The Journal of Physical Chemistry B*, 109(39):18218–18222, 2005. PMID: 16853342.

[29] Nikolaos E. Tsakoumis, Magnus Rønning, Øyvind Borg, Erling Rytter, and Anders Holmen. Deactivation of cobalt based fischer–tropsch catalysts: A review. *Catalysis Today*, 154(3–4):162 – 182, 2010. Eleventh International Symposium on Catalyst Deactivation , Delft(The Netherlands,) October 25-28, 2009.

[30] T. Nowitzki, A. F. Carlsson, O. Martyanov, M. Naschitzki, V. Zielasek, T. Risse, M. Schmal, H.-J. Freund, and M. Bäumer. Oxidation of alumina-supported co and co-pd model catalysts for the fischer-tropsch reaction. *The Journal of Physical Chemistry C*, 111(24):8566–8572, 2007.

[31] C.J. Weststrate, M.M. Hauman, D.J. Moodley, A.M. Saib, E. van Steen, and J.W. Niemantsverdriet. Cobalt fischer–tropsch catalyst regeneration: The crucial role of the kirkendall effect for cobalt redispersion. *Topics in Catalysis*, 54(13-15):811–816, 2011.

[32] B.A. Sexton, A.E. Hughes, and T.W. Turney. An {XPS} and {TPR} study of the reduction of promoted cobalt-kieselguhr fischer-tropsch catalysts. *Journal of Catalysis*, 97(2):390 – 406, 1986.

[33] H. Fredriksson, A. Alaverdyan, Y. Dmitriev, C. Langhammer, D.s. Sutherland, M. Zäch, and B. Kasemo. Hole-mask colloidal lithography. *Advanced Materials*, 19(23):4297–4302, 2007.

[34] Svetlana Syrenova, Carl Wadell, and Christoph Langhammer. Shrinking-hole colloidal lithography: Self-aligned nanofabrication of complex plasmonic nanoantennas. *Nano Letters*, 14(5):2655–2663, 2014. PMID: 24697350.

[35] John F. Moulder, William F. Stickle, Peter E. Sobol, and Kenneth D. Bomben. *Handbook of x-ray photoelectron spectroscopy*. Perkin-Elmer Corporation Physics electronics division, 1992.

[36] P. C. Thune, C. J. Weststrate, P. Moodley, A. M. Saib, J. van de Loosdrecht, J. T. Miller, and J. W. Niemantsverdriet. Studying fischer-tropsch catalysts using transmission electron microscopy and model systems of nanoparticles on planar supports. *Catal. Sci. Technol.*, 1:689–697, 2011.

[37] T.D Kang, H.S. Lee, and H. Lee. Optical properties of black nio and coo single crystals studied with spectroscopic ellipsometry. *KOREAN PHYSICAL SOCIETY*, 50(3):623–637, 2007.

[38] D. Barreca and C Massignan. Composition and microstructure of cobalt oxide thin films obtained from a novel cobalt(ii) precursor by chemical vapor deposition. *Chemical Materials*, (13):588–593, 2001.

[39] E.P. Surovoi, A.A. Sukhorukova, and S.V. Bin. General aspects of the growth of cobalt nanofilms during heat treatment. *Inorganic Materials*, 50(4):404–408, 2014.

[40] P. Tolédano, G. Krexner, M. Prem, H.-P. Weber, and V. P. Dmitriev. Theory of the martensitic transformation in cobalt. *Phys. Rev. B*, 64:144104, Sep 2001.

[41] A. L. Cabrera, B. C. Sales, and M. B. Maple. Oxidation of cobalt and iron near the $\epsilon \rightarrow \gamma$ and $\alpha \rightarrow \gamma$ structural phase transitions. *Phys. Rev. B*, 25:1688–1696, Feb 1982.

[42] Y.V. Kudryavtsev, V.V. Kokorin, L.E. Kozlova, V.N. Lermelenko, and S.M. Konoplyuk. Effect of martinistic transformation on the optical spectra of cu-mn-al alloy. *Material Science Forum*, 738-739:177–182, Jan 2013.

[43] Optical and electronic properties of metallic cobalt in various structural states. *Ukr. J. Phys*, 55(4).

[44] V.F. Drobny and L. Pulfrey. Properties of reactively-sputtered copper oxide thin films. *Thin Solid Films*, 61(1):89 – 98, 1979.

[45] P. B. Johnson and R. W. Christy. Optical constants of transition metals: Ti, v, cr, mn, fe, co, ni, and pd. *Phys. Rev. B*, 9:5056–5070, Jun 1974.

[46] R. J. Powell and W. E. Spicer. Optical properties of nio and coo. *Phys. Rev. B*, 2:2182–2193, Sep 1970.

[47] Bushra Kazim Hassun al MAyyali. Study the effect of thickness on the electrical conductivity and optical constant of co3o4 thin films. *Journal for Pure and Applied Science*, 26(1), 2013.

A

Appendix 1

A.1 Temperature-programmed oxidation and reduction of copper nanoparticles

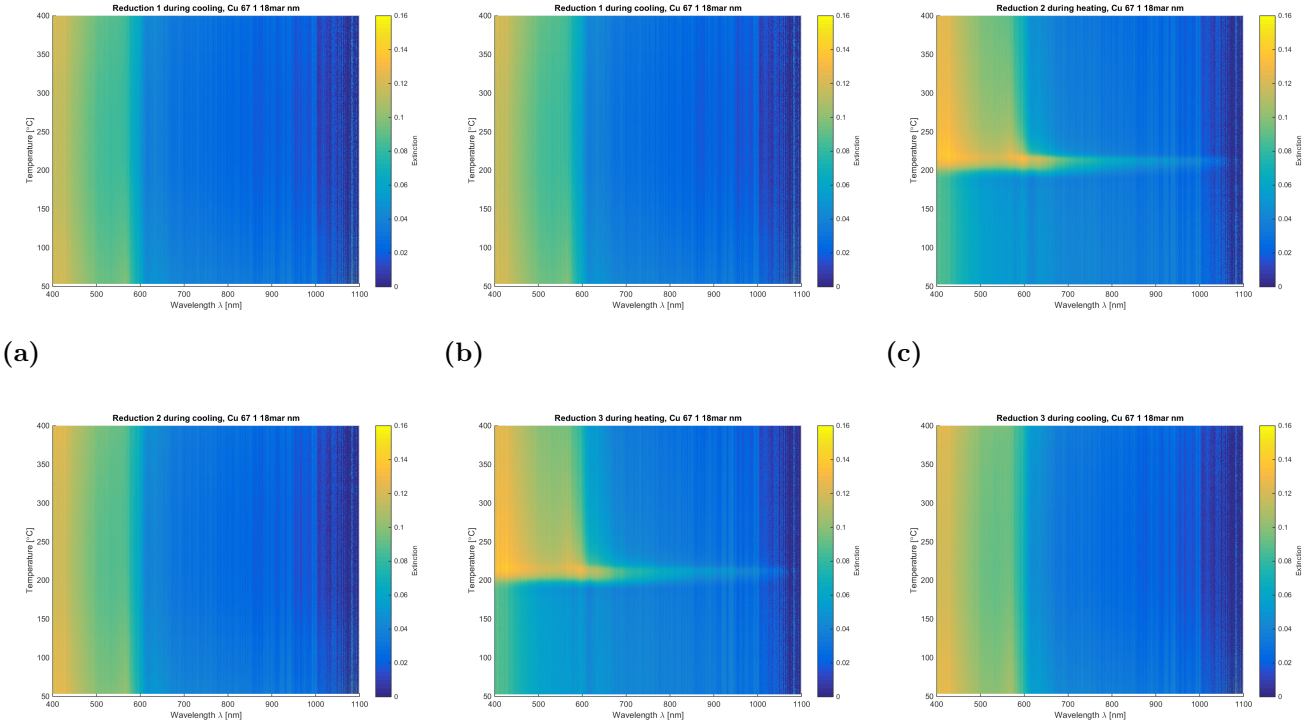

(a) **(b)** **(c)**

(d) **(e)** **(f)**

Figure A.1: Reduction cycles of Cu 67 nm

A.2 Temperature-programmed oxidation and reduction of cobalt nanoparticles

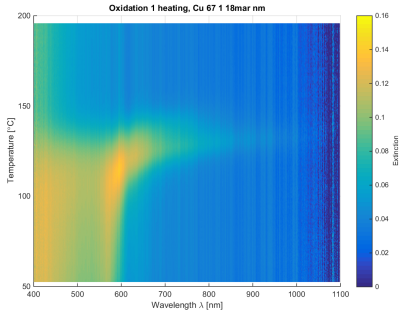

(a)

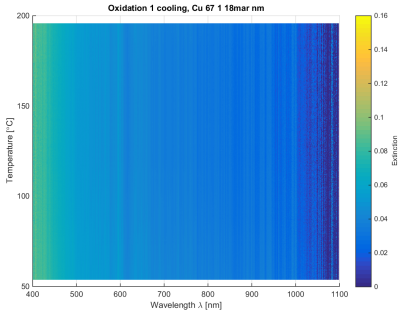

(b)

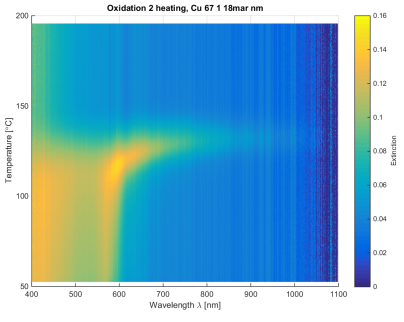

(c)

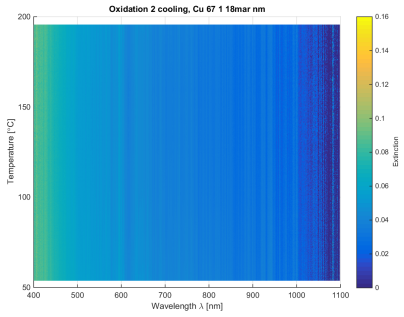

(d)

Figure A.2: Oxidation cycles of Cu 67 nm

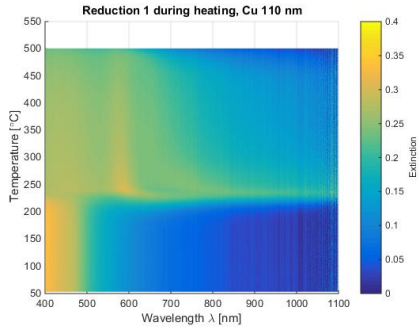

(a)

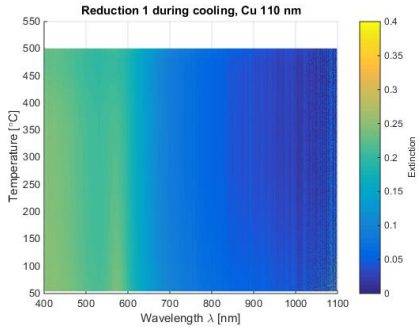

(b)

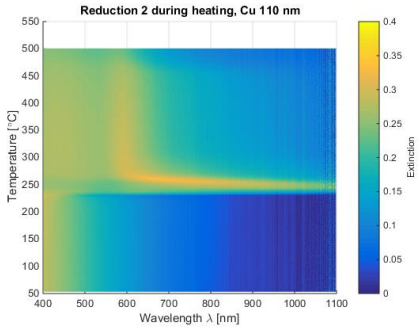

(c)

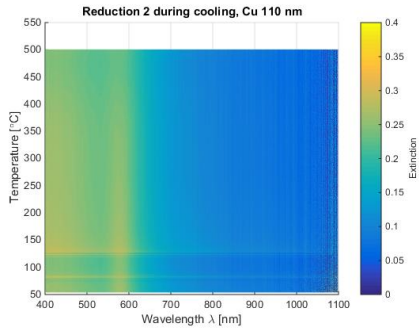

(d)

Figure A.3: Reduction cycles of Cu 110 nm

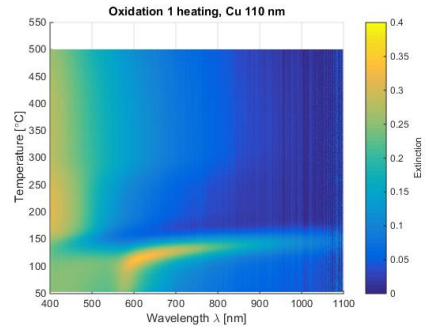

(a)

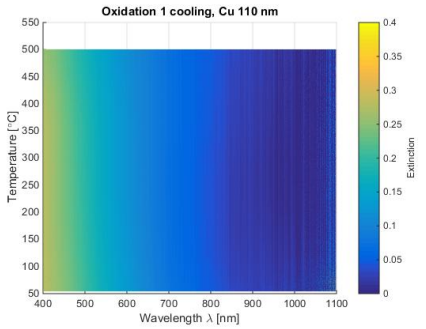

(b)

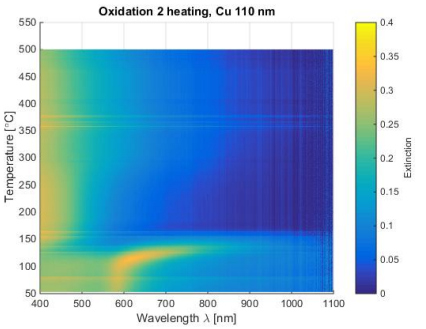

(c)

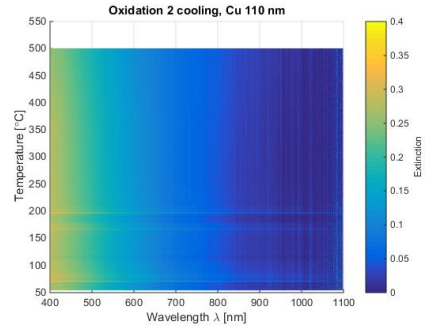

(d)

Figure A.4: Oxidation cycles of Cu 110 nm

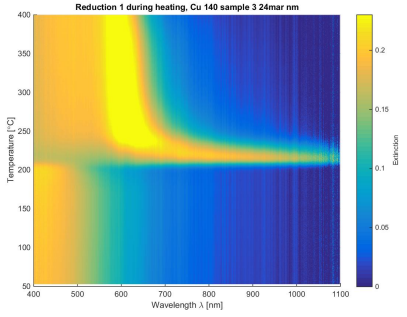

(a)

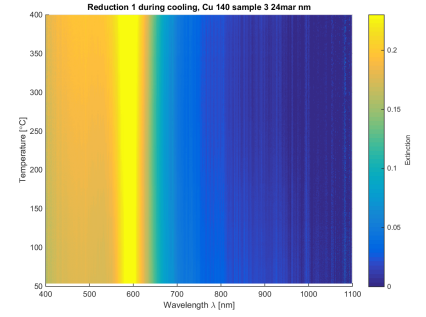

(b)

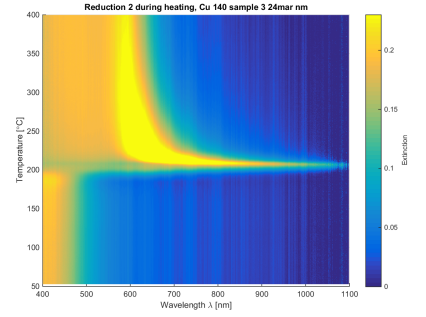

(c)

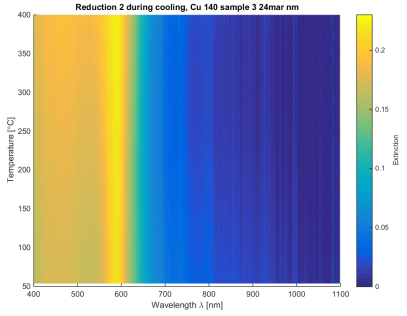

(d)

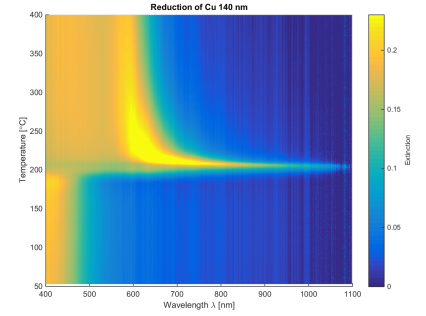

(e)

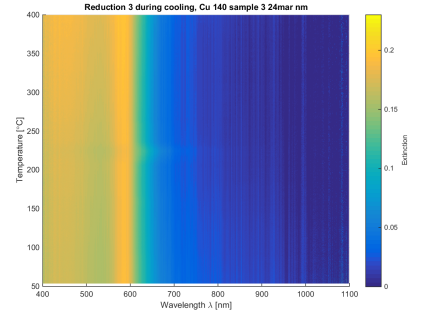

(f)

Figure A.5: Reduction cycles of Cu 140 nm

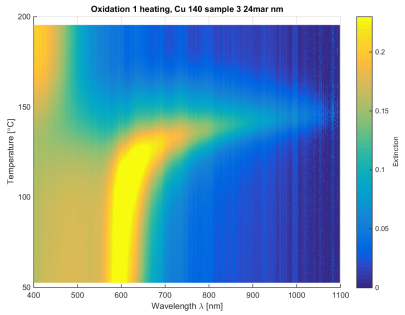

(a)

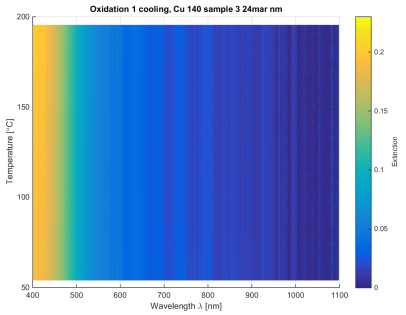

(b)

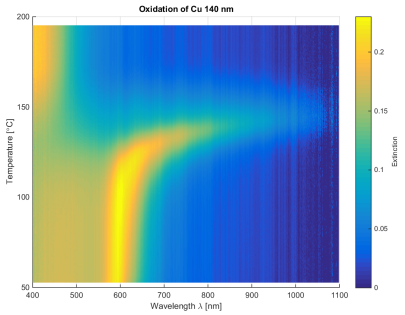

(c)

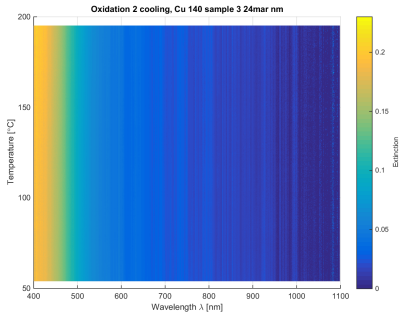

(d)

Figure A.6: Oxidation cycles of Cu 140 nm

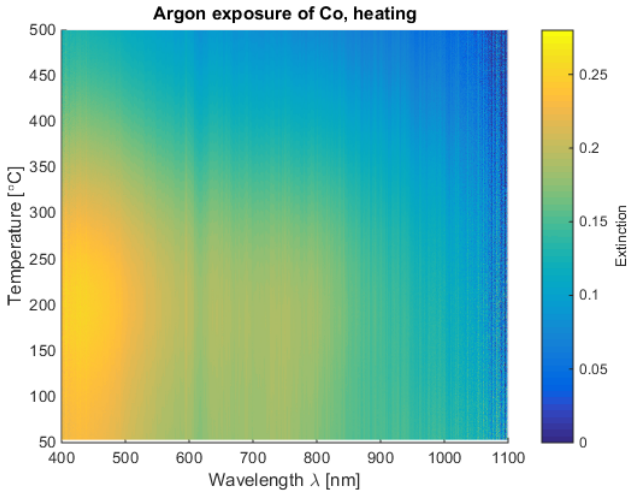

(a)

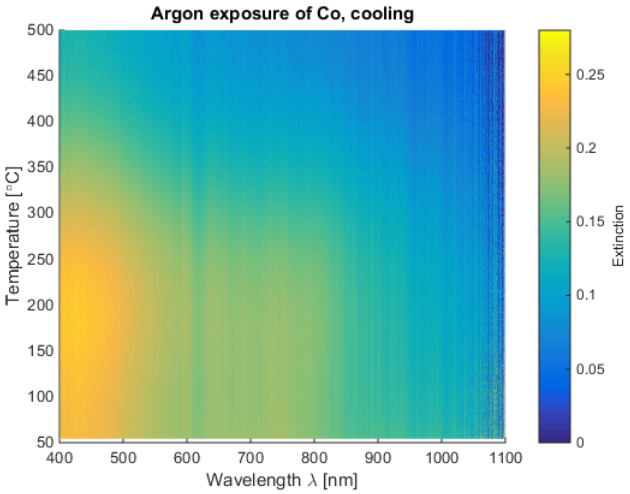

(b)

Figure A.7: Argon exposure of cobalt nanoparticles during (a) heating, and (b) cooling

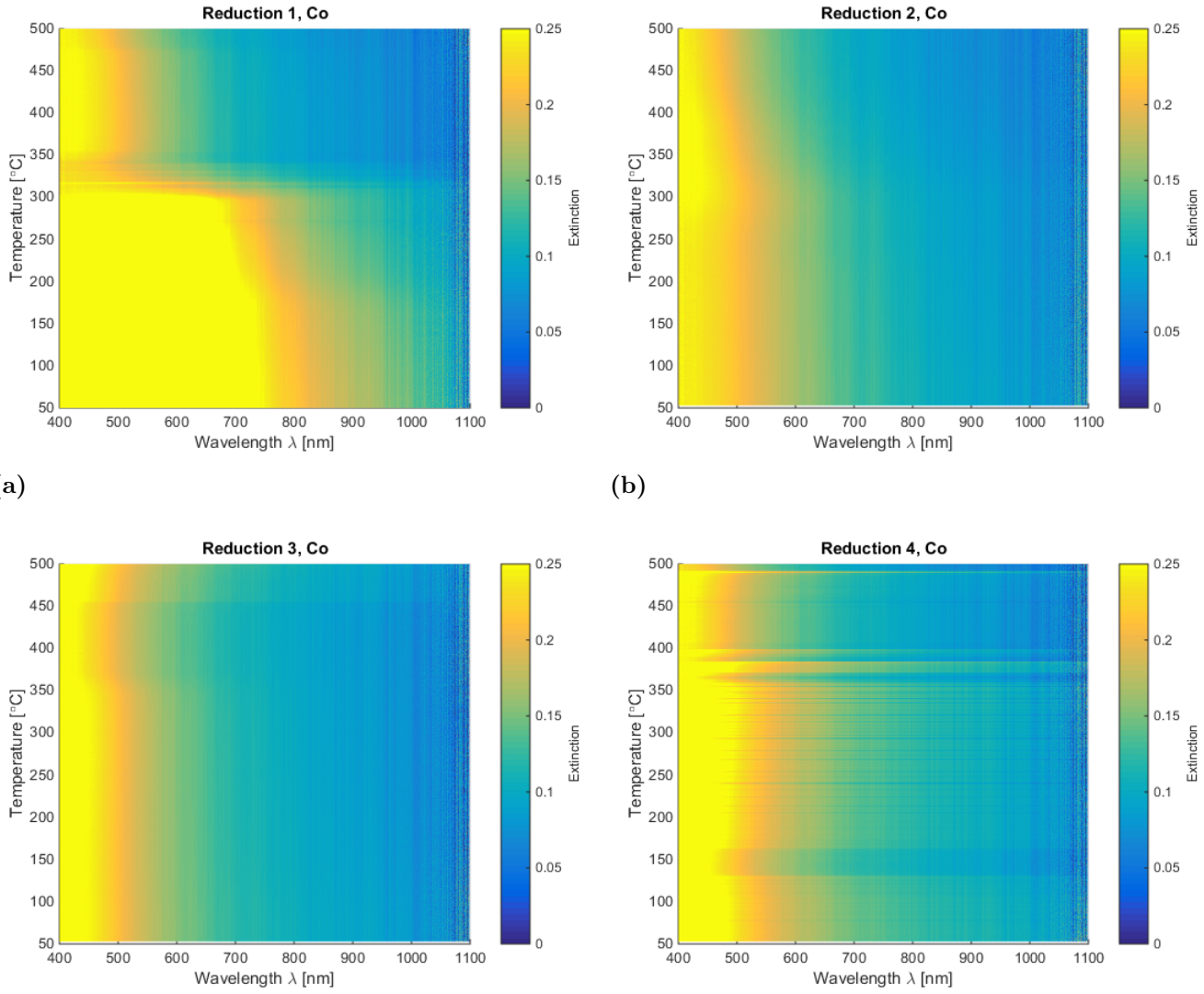

Figure A.8: Exposure of hydrogen during heating of cobalt nanoparticles. (a) is the first cycle of the experiment, (b) is the heating during hydrogen exposure right after the cooling of (a), (c) is the heating during hydrogen exposure right after the cooling of (b), (d) is the heating during hydrogen exposure right after the cooling of (c)

A.3 Temperature-programmed oxidation and reduction of cobalt film

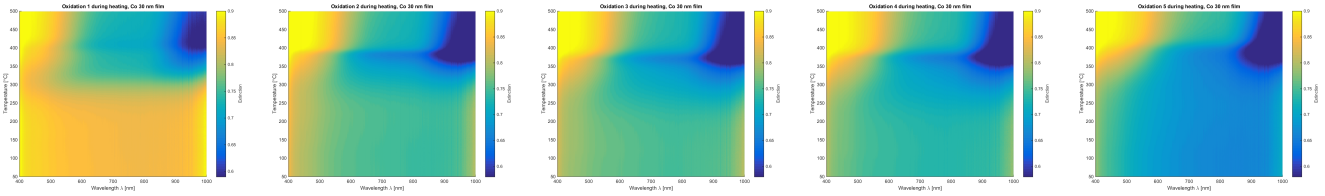

(a) **(b)** **(c)** **(d)** **(e)**

Figure A.9: Oxidation during heating Co film

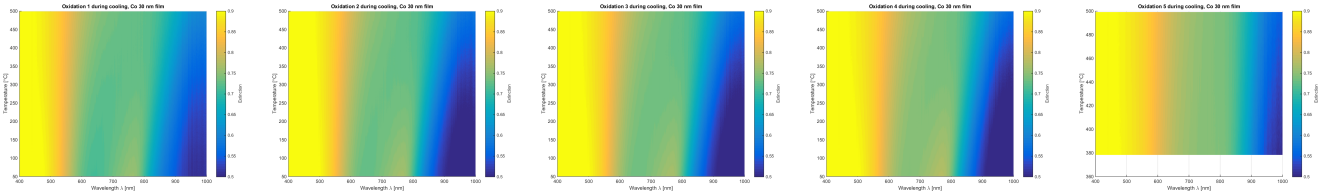

(a) **(b)** **(c)** **(d)** **(e)**

Figure A.10: Oxidation during cooling Co film

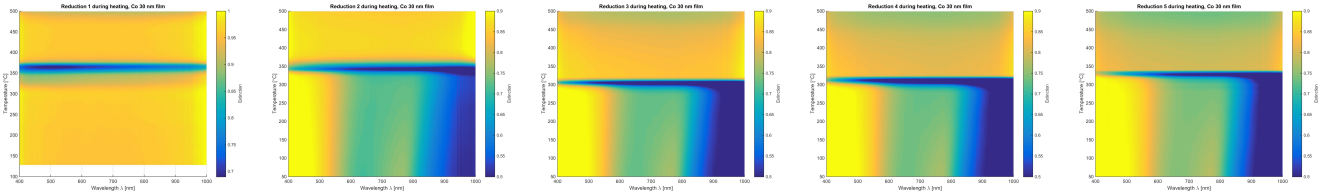

(a) **(b)** **(c)** **(d)** **(e)**

Figure A.11: Reduction during heating Co film

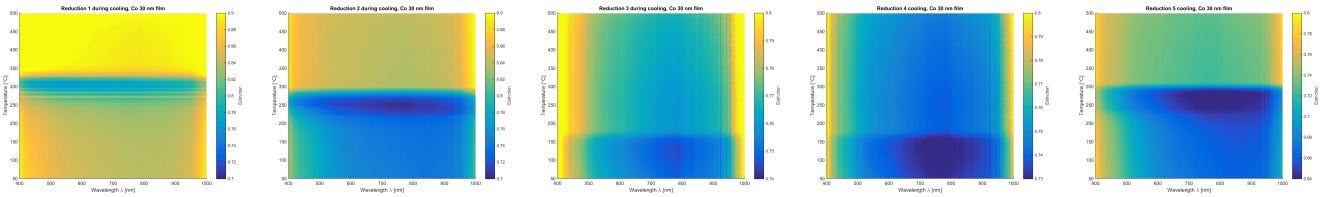

(a) **(b)** **(c)** **(d)** **(e)**

Figure A.12: Reduction during cooling Co film

A.4 Temperature ramps of Co film in Ar

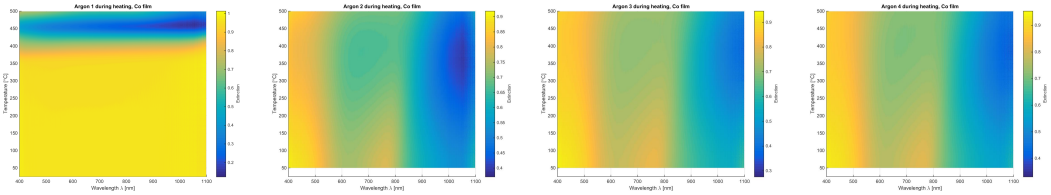

(a) **(b)** **(c)** **(d)**

Figure A.13: Argon exposure on Co film during heating

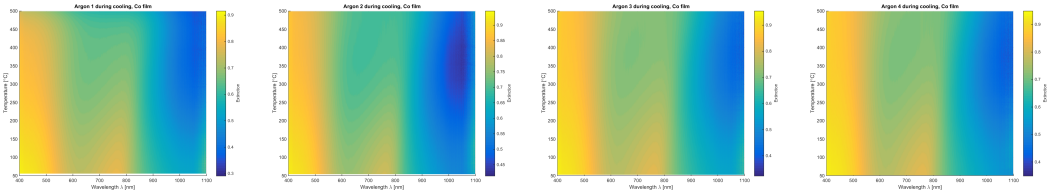

(a) **(b)** **(c)** **(d)**

Figure A.14: Argon exposure on Co film during cooling